

Copyright

by

Ye Chen

2010

The Thesis committee for Ye Chen

Certifies that this is the approved version of the following thesis

A Passive Wireless Sensor Array for Structural Health Monitoring

APPROVED BY

SUPERVISING COMMITTEE:

Supervisor: _____

Dean P. Neikirk

Andrea Alù

A Passive Wireless Sensor Array for Structural Health Monitoring

by

Ye Chen, B.E., M.E.

Thesis

Presented to the Faculty of the Graduate School of

The University of Texas at Austin

in Partial Fulfillment

of the Requirements

for the Degree of

Master of Science in Engineering

The University of Texas at Austin

May 2010

Acknowledgements

I would like to thank my advisor, Dr. Dean P. Neikirk for his instructive advice on this thesis and my work with him. Dr. Dean P. Neikirk has been an invaluable resource both as a technical advisor and mentor. I do benefit much from discussions with him and I believe he helped improve the quality of my work immensely. He is very patient, affable and accommodating. I am thankful to have an opportunity to work with him.

I would also like to thank Praveen Pasupathy for his patience and assistance with technical and experimental questions. He helped me be easy and enjoyable when facing hard part of my work. I also appreciate the help of other members in Team Neikirk for the help in experiment and always being there to answer questions.

I thank Dr. Sharon Wood and her students at the Ferguson Structural Engineering Laboratory, who give me an insight on the knowledge about corrosion of concrete and make me better involved in the corrosion sensor design.

I also want to thank Dr. Andrea Alù to be the reader of my thesis. The study experience in his graduate course Electrodynamics gives me inspiration for this thesis.

I would also like to thank my parents and friends for their continual support throughout my life and study. Your love makes me what I am today.

May 2010

Abstract

A Passive Wireless Sensor Array for Structural Health Monitoring

Ye Chen, M.S.E

The University of Texas at Austin, 2010

Supervisor: Dean P. Neikirk

This thesis summarizes ongoing work to develop low-cost, wireless, resonant sensor array that can be used to monitor corrosion in infrastructure systems. A magnetically coupled sensor array is presented and analyzed using circuit model. The array acts as a magneto-inductive waveguide and the impedance discontinuities caused by corrosion (or other defects) lead to reflection. The relationship between the relative position of defects and pass band characteristics is investigated, providing a technique to determine the location of targets. A configuration for increased sensitivity and a method for defect localization are presented.

Table of Contents

CHAPTER 1	INTRODUCTION	1
1.1	Corrosion of Civil Engineering Infrastructure	1
1.2	Methods for Detecting Corrosion in Concrete	1
1.2.1	Visual Inspection	2
1.2.2	Open Circuit Potential Measurement	2
1.2.3	Concrete Resistivity Measurement.....	3
1.2.4	Ultrasonic Pulse Velocity Measurement.....	3
1.2.5	Embedded Wireless Sensors.....	4
1.3	Large Scale Surveillance in Structural Health Monitoring	5
1.3.1	Wired Sensor Network	5
1.3.2	Wireless Sensor Network	6
1.4	Scope of Research Work	7
CHAPTER 2	DEVELOPMENT OF 1-D CORROSION SENSOR ARRAY	9
2.1	Introduction	9
2.2	Passive Wireless Corrosion Sensors.....	9
2.2.1	Circuit Model	10
2.2.2	Self Inductance.....	13
2.2.3	Mutual Inductance.....	18
2.3	1-D Corrosion Sensor Array.....	23
2.3.1	Circuit Model	23
2.3.2	Dispersion Relationship	26
2.3.3	Matched Impedance	32
2.3.4	Insertion Loss	34
2.4	Summary	39
CHAPTER 3	SENSING MECHANISM OF 1-D PASSIVE CORROSION SENSOR ARRAY	41
3.1	Introduction	41
3.2	1-D Corrosion Sensor Array with One Defect	41
3.2.1	Circuit Model	42
3.2.2	Frequency Characteristics	43
3.3	1-D Corrosion Sensor Array with Two Defects	49
3.3.1	Circuit Model	49
3.3.2	Frequency Characteristics	53
3.4	Sensing Mechanism	59
3.5	Summary	64
CHAPTER 4	EXPERIMENTAL RESULTS IN THE AIR	66
4.1	Introduction.....	66
4.2	Basic Set Up.....	66

4.3	Test of 1-D Corrosion Sensor Array.....	68
4.3.1	Test of Intact 1-D Corrosion Sensor Array.....	68
4.3.2	Test of 1-D Corrosion Sensor Array with One Defect	72
4.3.3	Test of 1-D Corrosion Sensor Array with Two Defects.....	75
4.4	Summary	78
CHAPTER 5 CONCLUSION		80
5.1	Motivation of Work.....	80
5.2	Simulation and Results.....	81
5.2.1	Intact 1-D Corrosion Sensor Array.....	81
5.2.2	1-D Corrosion Sensor Array with One Defect	81
5.2.3	1-D Corrosion Sensor Array with Two Defects.....	82
5.3	Recommendation for the Future.....	82
Bibliography		84
Vita.....		87

List of Figures

Figure 2.1 Prototype of passive wireless corrosion sensor	10
Figure 2.2 Schematic diagram of sensing platform.....	10
Figure 2.3 Circuit model of sensing platform	11
Figure 2.4 Magnitude and phase of input impedance	12
Figure 2.5 Magnitude and phase of input impedance with increasing resistance	13
Figure 2.6 Schematic diagram of an inductive coil.....	14
Figure 2.7 Self inductance vs. Number of Turns.....	16
Figure 2.8 Self inductance vs. Radius.....	17
Figure 2.9 Configuration of coaxial coils.....	19
Figure 2.10 Mutual inductance vs. Distance for coaxial coils	20
Figure 2.11 Mutual inductance vs. Number of turns for coaxial coils	20
Figure 2.12 Configuration of coplanar coils	21
Figure 2.13 Mutual inductance vs. Distance for coplanar coils	22
Figure 2.14 Mutual inductance vs. Number of turns for coplanar coils.....	22
Figure 2.15 Schematic diagram and circuit model of passive wireless sensor array	24
Figure 2.16 Dispersion relationship for coaxial sensor array with $d=2.54\text{cm}$	28
Figure 2.17 Dispersion relationship for coplanar sensor array with $d=1\text{cm}$	28
Figure 2.18 Coupling factor vs. Distance for coaxial and coplanar coils.....	31
Figure 2.19 Passband width vs. Distance for coaxial and coplanar sensor arrays	31
Figure 2.20 Current distribution for 18-element passive sensor array at $\beta d=\pi/3$	34
Figure 2.21 Insertion loss vs. Normalized frequency for coaxial sensor array with different number of elements	36
Figure 2.22 Insertion loss vs. Normalized frequency for coplanar sensor array with different number of elements	37
Figure 2.23 Insertion loss vs. Normalized frequency for coaxial sensor array with different axial spacing	38
Figure 2.24 Insertion loss vs. Normalized frequency for coplanar sensor array with different gap	39
Figure 3.1 Schematic diagram and circuit model of 1-D sensor array with one defect	42
Figure 3.2 Schematic diagram of 1-D sensor array with one defect	44
Figure 3.3 Power reflection and transmission coefficient vs. Mutual inductance ratio	45
Figure 3.4 Power reflection and transmission coefficient vs. normalized frequency.....	46
Figure 3.5 Power reflection and transmission coefficient vs. Normalized frequency for contact coaxial and coplanar sensor array	47
Figure 3.6 Insertion loss vs. Normalized frequency for coaxial and coplanar sensor array with one defect.....	48
Figure 3.7 Schematic diagram and circuit model of 1-D sensor array with two adjacent defects	50

Figure 3.8 Insertion loss vs. Normalized frequency for coaxial sensor array with different number of elements	50
Figure 3.9 Insertion loss vs. Normalized frequency for coplanar sensor array with different defects	51
Figure 3.10 Schematic diagram and circuit model of 1-D sensor array with two defects.....	51
Figure 3.11 Schematic diagram of 1-D sensor array with two distributed defects.....	53
Figure 3.12 Power reflection and transmission coefficient vs. Normalized frequency for coaxial sensor array with two discontinuities	55
Figure 3.13 Power reflection and transmission coefficient vs. Normalized frequency for coplanar sensor array with two discontinuities	56
Figure 3.14 Power reflection and transmission coefficient vs. Normalized frequency with different quality factors at resonant frequency.....	57
Figure 3.15 Insertion loss vs. Normalized frequency for coaxial sensor array with two discontinuities	58
Figure 3.16 Insertion loss vs. Normalized frequency for coplanar sensor array with two discontinuities	59
Figure 3.17 Insertion loss vs. Normalized frequency for coaxial sensor array with two defects ..	61
Figure 3.18 Insertion loss vs. Normalized frequency with the second or second-to-last element as reference reflector	62
Figure 3.19 Insertion loss vs. Normalized frequency for coaxial sensor array with second corrosion sensor as reference reflector.....	63
Figure 3.20 Insertion loss vs. Normalized frequency for coplanar sensor array with second corrosion sensor as reference reflector.....	64
Figure 4.1 Input impedance characteristics of coil	67
Figure 4.2 1-D magnetically coupled passive wireless sensors as MI waveguides	68
Figure 4.3 Experimental arrangement of 1-D coaxial sensor array.....	69
Figure 4.4 Insertion Loss vs. Normalized frequency of 1-D coaxial sensor array with $d=2.54\text{cm}$	70
Figure 4.5 Insertion Loss vs. Normalized frequency for 1-D coaxial sensor array.....	71
Figure 4.6 Minimum loss vs. Number of sensors of 1-D coaxial sensor array	72
Figure 4.7 Insertion Loss vs. Normalized frequency for 1-D coaxial sensor array with No.3 defect	73
Figure 4.8 Insertion Loss vs. Normalized frequency for 1-D coaxial sensor array with No.3 defect	74
Figure 4.9 Insertion Loss vs. Normalized frequency for 1-D coaxial sensor array with one defect	75
Figure 4.10 Frequency responses of 1-D coaxial sensor array with two defects ($P=3$)	76
Figure 4.11 Insertion Loss vs. Normalized frequency for 1-D coaxial sensor array with different sets of two defects	77
Figure 4.12 Verification of peaks locations for $P=5$ and $P=8$	78

CHAPTER 1 INTRODUCTION

1.1 Corrosion of Civil Engineering Infrastructure

Corrosion of embedded reinforcing steel is a worldwide problem. Corrosion degrades the integrity of the steel and decrease the lifespan of the infrastructure. The ingress of chloride ions and carbon dioxide are the major contributing factors of corrosion, and structures located in the coastal marine environment are more vulnerable to this damage. After the steel begin to corrode, the corrosion products are deposited around the reinforcing steel. Within the limited space, crack and spalling will occur resulting from the expansive stresses of increased corrosion product.

Each year almost 23 billion dollars is spent on replacing and repairing the structurally deficient highway bridges due to corrosion. The indirect cost resulting from traffic delays and lost productivity are approximately ten times as this amount [1]. An early detect of corrosion not only extend the service lift of structures but also significantly decrease the costs of maintaining structures.

1.2 Methods for Detecting Corrosion in Concrete

Many electrochemical and non-destructive techniques exist for corrosion monitoring in reinforced concrete. Each of them possess with certain advantages and limitations. The current methods are summarized in this section.

1.2.1 Visual Inspection

Visual inspection is most basic and traditional method. It is conducted by inspecting the structures visually. The periodic inspection covers the information as crack, spalling, rust staining and so on [2]. However, crack and spalling can be detected visually until it extends to surface, which means extreme expensive repairs even replacement is needed to recover the structure. Sometimes tools like hammers are used to help check the soundness of concrete. The hollow sound indicates that cracks have formed inside. This method can detect cracks before they reach the surface of the concrete. The advantages of visual inspection are low cost and ability to detect the early signs of corrosion.

1.2.2 Open Circuit Potential Measurement

Another commonly used method is open circuit potential measurement. In reinforced concrete structures, concrete acts as an electrolyte and form electrochemical half-cell with exposed rebar. The potential between them is affected by the surrounding environment. The principle involved in this technique is that the potential is measured with respect to standard reference electrode, such as saturated calomel electrode (SCE), copper sulfate electrode (CSE), and etc. The relationship between corrosion condition and open circuit potential (OCP) value are listed in ASTM C876 [3]. OCP values can provide just information for corrosion probability but corrosion rate [4].

1.2.3 Concrete Resistivity Measurement

Another electrical technique is measuring electrical resistivity of concrete, which is related to determination of intensity of the initiated corrosion process. Low resistivity indicates high risk of corrosion condition in reinforced concrete, since the current can easily pass between anode and cathode areas. The study shows that concrete resistivity measurement was an effective parameter to evaluate the risk of reinforcing steel corrosion [5]. The relation between corrosion condition and resistivity is presented by a number of authors [6]. The resistivity measurement is a useful additional measurement to aid in detecting problem areas or confirming concerns about poor quality concrete, since rebar will interfere with resistivity measurements.

1.2.4 Ultrasonic Pulse Velocity Measurement

Ultrasonic pulse velocity measurement is another non destructive technique. The principle is based on measuring the speed of sound through materials under test. A pair of transmitter and receiver is used to generate and receive the ultrasonic waves. The time interval T spent by wave propagation is precisely measured by electronic instrument. However, since phase velocity is also affected by a lot of other elements, it is not easy to interpret test data [7].

1.2.5 Embedded Wireless Sensors

In recent years, there is an increasing application of sensing technologies in structural health monitoring. A benefit of embedded wireless sensors is that they can provide the measurement data when it is not accessible. However, a challenge embedded sensors face is the finite lifetime of battery. Radio frequency identification technology is adopted to solve this problem, which is used to communicate data and power sensors at the same time. The interrogators transmit power source through inductive magnetic coupling.

Carkhuff and Cain have proposed a passive RFID-based wireless sensor to monitor corrosion [8]. The prototype sensor includes two inductive coils. One of the coils is to obtain power from interrogators by mutual coupling. Another coil behaves as an antenna for wireless communication.

A design of a passive RFID-based corrosion sensor which makes use of MEMS sensors are developed by Saafi and Romine [9]. The MEMS sensor is designed to monitor several parameters-pH, relative humidity, and the concentration of chloride ions and CO₂. The interrogator is able to communicate with the sensor at a distance of 1.5cm above the concrete bridge deck when sensors is placed 2.5 cm below member surface.

Novak et al. from University of Texas at Austin proposed a passive wireless corrosion sensor, which utilized an inductor-capacitor resonant circuit [10]. The proposed sensor can complete wireless transmission of data and measurement of corrosion

thresholds. The involved principle is the resonant frequency shift associated with corrosion situation inside concrete. An extensive and successful laboratory tests are conducted by Simonen et al., where the proposed wireless sensor is embedded in large-scale concrete slabs exposed to various levels of chloride ingress [11]. Andringa et al. have further presented a series of additional laboratory tests [12] and Nainani adopted genetic algorithm [13] that allow them to optimize the design of the wireless corrosion state sensor. Praveen et al. proposed a new structure including a sacrificial layer to detect onset of corrosion [14] The passive wireless corrosion sensors are effective in monitoring corrosion and they are extremely simple and low cost for a large scale deployment.

1.3 Large Scale Surveillance in Structural Health Monitoring

Development of health monitoring system could provide real-time information of existing reinforced concrete structures in a large scale from distributed nodes. Wired and wireless sensor systems have been developed to monitor corrosion condition in civil infrastructure.

1.3.1 Wired Sensor Network

The Embedded Corrosion Instrument (ECI) is an electronic corrosion sensor that provides early warning of conditions that damage steel reinforcement, leading to cracking, spalling, and other deterioration of concrete structures [15]. Each node monitors five key factors: linear polarization, resistance, open circuit potential, resistivity, chloride ion

concentration and temperature, which provide comprehensive information on corrosion conditions. All embedded ECI are components of a local area network. Each ECI is connecting to a datalogger using a three-wire sensor. The dataloggers are responsible for collecting and processing the measurements output from sensors, which can be downloaded to a local computer or transmitted through wireless network [15].

Coaxial wires are employed in this structural monitoring system for communications between sensors and repository. Wired network can guarantee that measurements data are collected and distributed reliably. But wires have to be deployed all over the structure. Their installation in structure can be expensive and maintenance could be labor-intensive.

1.3.2 Wireless Sensor Network

The high cost by the installation of wired sensors can be reduced by taking advantage of wireless sensors, since wires are no longer needed for connections between sensors and data acquisition system. Recently wireless sensors and wireless sensor network are emerging as effective techniques substituting for traditional health monitoring methods.

A large number of wireless sensor platforms have emerged that are designed for use in structural health monitoring application. The Mote wireless sensor platform developed by University of California-Berkeley receives great attention, since both software (TinyOS [16]) and hardware are open source to the public. Systems based on

Mote have been deployed in a number of large-scale monitoring applications. For example, over 150 Motes have been implemented to monitor the weather and nesting condition of birds on Great Duck Island [17]. 59 nodes are distributed over the span and the tower of Golden Gate Bridges to supervise acceleration of the structure [18]. Crossbow MicaZ motes are used for control and communication of accelerometers. For a reliable data collection, Straw provided 461B/s bandwidth to a node 44 hops away [19].

Praveen et al. have developed a passive wireless sensor net consisting of a line of resonant Electronic Article Surveillance (EAS) tags to monitor large areas [12]. Experimental results show that the resonant sensor net has band-pass characteristics and acts as a magneto-inductive waveguide (MIW). Defects are introduced by covering tags with conductive paper. The presence of defects changes band-pass characteristics of sensor net. The frequency characteristics of 2-D resonant net is also studied and proved to have high sensitivity in detecting a single defect.

1.4 Scope of Research Work

The objective of this thesis is to develop a prototype 1-D linear wireless corrosion sensor array to detect corrosion in reinforced concrete structures. The 1-D corrosion sensor array will extend the coverage of point corrosion sensors for large scale surveillance in civil infrastructures. The sensors arrangement will help researchers to locate and detect corrosion through frequency variations instead of interrogating the impedance characteristics of sensors individually.

Chapter 2 reviews the wireless passive resonant corrosion sensors developed at University of Texas at Austin to make reader better understand the structure of 1-D sensor array. The dispersion relationship and frequency characteristics of coaxial and coplanar 1-D corrosion sensor array as a MI waveguide are then explored in Chapter 2. Chapter 3 discusses the sensing mechanism of 1-D corrosion sensor array associated with its frequency characteristics. The methods for locating the defect caused by corrosion in the line of sensors are provided. Chapter 4 covers the development of prototype 1-D corrosion sensor array. The sensor arrays are tested in a laboratory environment and the experimental results are presented. Chapter 5 summarizes the thesis and provides some suggestions for the future research.

CHAPTER 2 DEVELOPMENT OF 1-D CORROSION SENSOR ARRAY

2.1 Introduction

The purpose of this chapter is to present developed passive corrosion sensors and development of passive wireless sensor array for structural health monitoring, specifically corrosion in concrete. The relationship between sensor array structure and frequency characteristics of the passive wireless sensor array will be investigated.

2.2 Passive Wireless Corrosion Sensors

The low-cost passive wireless corrosion sensors have been developed to monitor corrosion of reinforced steel concrete at the University of Texas at Austin[2, 10, 11, 20, 21]. The corrosion sensors are hermetically sealed and embedded in the concrete. External reader is used to both communicate and power corrosion sensor by linked magnetic flux. Without the need for batteries, the sensors can conceivably work as long as the lifetime of the structures which they are designed to monitor. The epoxy enclosure enables corrosion sensors to survive concrete curing and withstand the harsh environment inside concrete. A sensor prototype is presented as follows [21]:

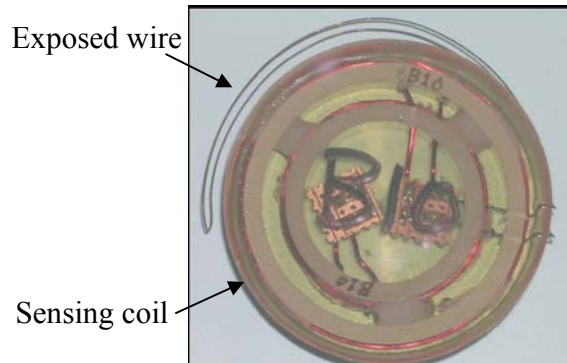


Figure 2.1 Prototype of passive wireless corrosion sensor

2.2.1 Circuit Model

The passive wireless corrosion sensor utilizes an inductor-capacitor circuit to allow a remote wireless reader to power the sensor and receive measurement data. Each sensor is constructed by a coil, a capacitor and an exposed wire as resistive transducer. The reader is an inductive coil that magnetically coupled to the coil in corrosion sensor circuit, as presented in Figure 2.2 [21].

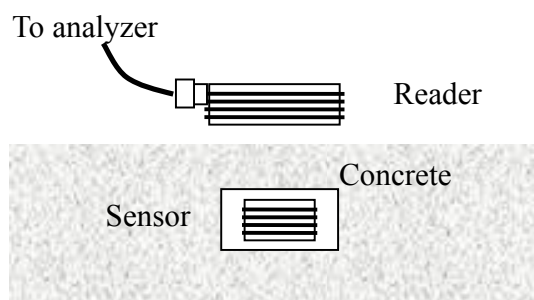


Figure 2.2 Schematic diagram of sensing platform

The circuit model of sensing system is shown in Figure 2.3. The reader coil is simplified as an inductance. The corrosion sensor circuit is idealized as a RLC resonant

circuit. R , L and C indicate the circuit resistance, inductance of coil and additional capacitance that make sensor a resonant circuit. The reader and sensor are coupled by the mutual inductance M .

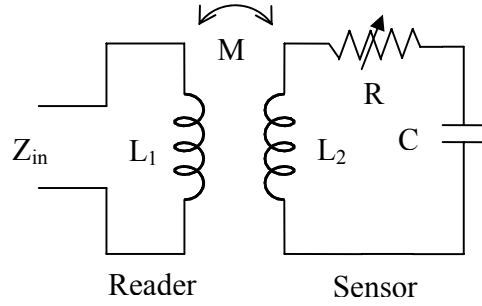


Figure 2.3 Circuit model of sensing platform

The passive corrosion sensor is a resonant circuit with resonant frequency of f_0 , as expressed in Equation (2.1). The resonance is manifested as an inflection point in the magnitude and a dip in the phase at the sensor circuit resonant frequency by measuring the input impedance Z_{in} [22], as shown in the Figure 2.4. The x-coordinate indicates frequency normalized with f_0 .

$$f_0 = \frac{1}{2\pi\sqrt{L_2C}} \quad (2.1)$$

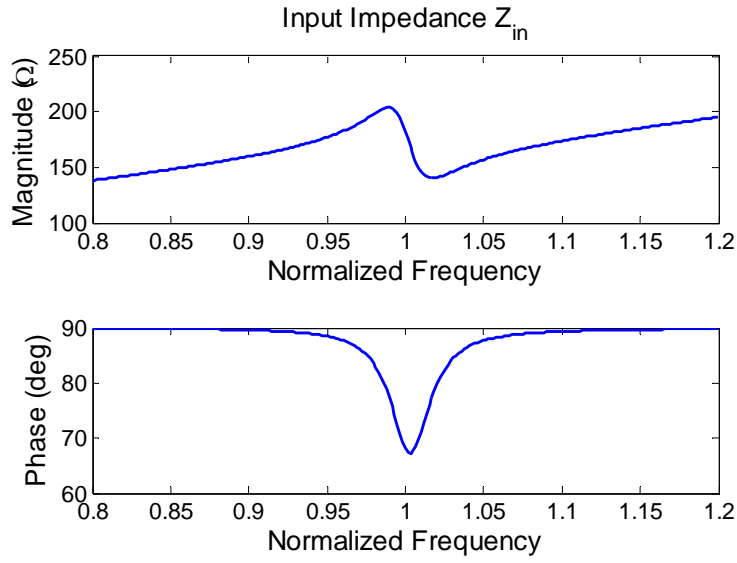


Figure 2.4 Magnitude and phase of input impedance

The equation for input impedance is expressed as,

$$Z_{in} = j\omega L_1 + \frac{(\omega M)^2}{R + j\left(\omega L_2 - \frac{1}{\omega C}\right)} \quad (2.2)$$

where L_1 and L_2 are the self inductance of read and sensor coil. A simple threshold sensor is developed by using the circuit model [2]. The characteristics of input impedance depend on configuration of sensor circuit when the reader is fixed. The principle involved in the sensor design is based on corresponding change in measured impedance associated with variance of circuit component. The wire resistance will increase as the exposed wire is corroded, which will caused a reduction in and magnitude and depth of the input impedance phase dip, as presented in Figure 2.5. After the exposed wire is corroded broken, the input impedance magnitude will only proportional to self inductance of reader L_1 and phase dip will disappear. The wire exposed in the same corrosive

environment as the reinforcing steel acts as a resistive transducer in this sensor.

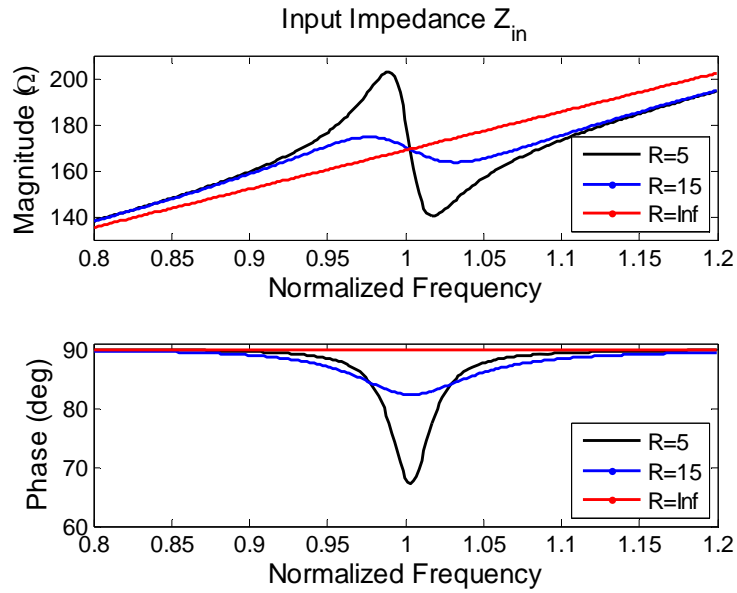


Figure 2.5 Magnitude and phase of input impedance with increasing resistance

2.2.2 Self Inductance

The self inductance is intrinsic characteristics of inductive coil, which relate to the configuration of coil. The self inductance is defined as the ratio of magnetic flux Φ to current I . The inductors used in experiment are wire coils. We assume the coil has radius a , length l and number of turns N , whose configuration is shown in Figure 2.6.

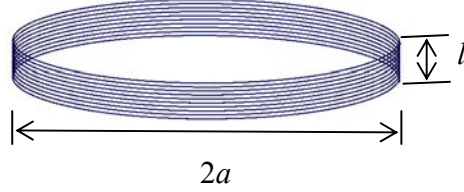


Figure 2.6 Schematic diagram of an inductive coil

Several approximation methods can be used to predict the self inductance of coils. A well-known method is the loop model [23], which divide the N -turn helical coil into N loops. Each loop has the same radius as the original coil and spaced by the pitch with its adjacent loops. The inductance is given by the sum of self inductance L_i ($i=1,2,\dots,N$) and mutual inductance M_{jk} ($j,k=1,2,\dots,N$) between any two loops. This model is not accurate with loosely-wound coils since helical effects are neglected. The Nagaoka's formula was chosen to calculate self inductance of helical coils in [13]. The formula are presented as follows,

$$L = 0.002\pi^2 a \left(\frac{2a}{b} \right) N^2 K \quad (2.3)$$

where a and b is the coil radius and length in centimeters, and K is a corrected factor as,

$$K = \frac{2\beta}{\pi} \left[\left(\ln \frac{4}{\beta} - \frac{1}{2} \right) + \frac{\beta^2}{8} \left(\ln \frac{4}{\beta} + \frac{1}{8} \right) - \frac{\beta^4}{64} \left(\ln \frac{4}{\beta} - \frac{2}{3} \right) + \dots \right] \quad (2.4)$$

where β equals to $b/2a$.

In this thesis, BiotSavart software is used to calculate the self inductance of a

helical coil. The magnetic flux Φ is computed from the vector potential $A(r)$ by the volume integral [24],

$$\Phi = \int dVA \cdot W \quad (2.5)$$

where W is the vector winding density. The integral are done by a sum of magnetic flux Φ value at M points, where M can be adjusted by the user. Then self-inductance will be computed according to its definition.

To use the BiotSavart Software, the wire coil structure is drawn first by inputting graphical commands in Make conductor>Wire. Graphical user interface will display the coil configuration according to the code. Resolution and Linked flux are set as 0.001. Since the coil is tightly-wound, pitch is assumed having the same value as diameter which depends on chosen wire gauge. After setting the current value 0.01 in Modify>Current, the self inductance can be obtained by clicking Self-inductance button at Calc tab. The results of different radius and number of turns are presented in following figures. The 22 AWG wire is chosen to make the inductor.

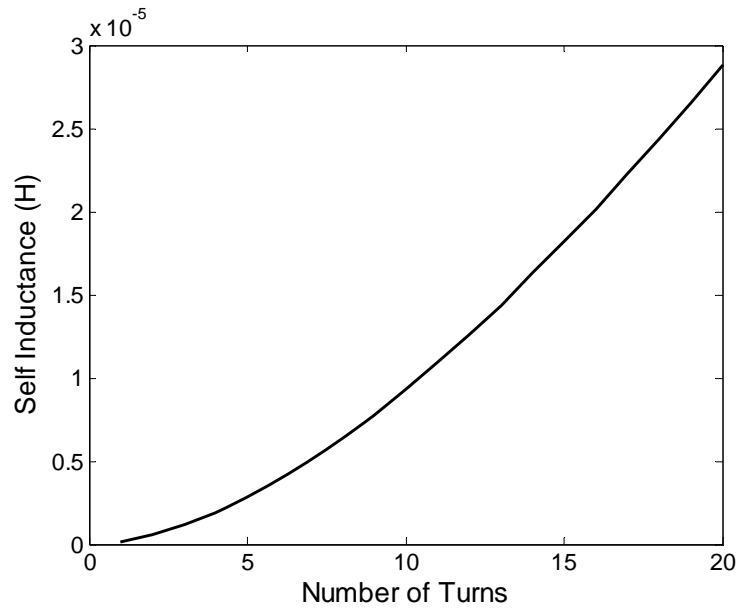


Figure 2.7 Self inductance vs. Number of Turns

Figure 2.7 shows the relationship between the number of turns and self inductance, while the coil radius is fixed at one inch (2.54cm). In this calculation, the pitch between turns is 0.6452mm, and the coil length equals to product of pitch and number of turns. We can see that the more turns in a coil, the greater the inductance.

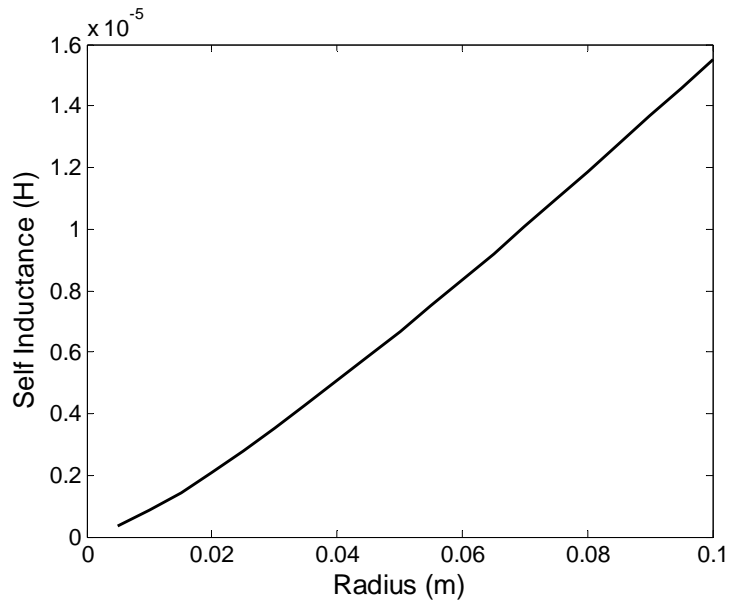


Figure 2.8 Self inductance vs. Radius

The variation of self inductance as the coil radius changes is presented in Figure 2.8. The self inductances of these 5-turn coils go up with greater radius.

The calculated results are compared with the measured results, as listed in Table 2.1. L_B indicates the value computed by BiotSavart software. The measurement data is listed in the column of $L_{measured}$. From the comparison, we can see that BiotSavart software can give an accurate approximation to self inductance.

Table 2.1 Calculated vs. Measured self inductance

Radius (m)	Length (m)	Turns	L_B (μH)	$L_{measured}$ (μH)
0.021	0.002	5	2.54	2.7[13]
0.021	0.004	10	8.44	8.4[13]
0.028	0.0015	3	1.42	1.4[13]

2.2.3 Mutual Inductance

In this sensing system, the reader and the sensor are connected by the magnetic coupling. The strength of the coupling will decide the maximum depth that the corrosion sensor can be embedded at [13]. Mutual inductance is defined as the ratio of the linked magnetic flux to the current in one coil, which can be expressed as,

$$M = \frac{\Lambda_{12}}{I_1} = \frac{N_2}{I_1} \int_{s_2} \vec{B}_1 \cdot d\vec{s} \quad (2.6)$$

where Λ_{12} is the linked flux in Coil 2 induced by the current I_1 in Coil 1, N_2 is the number of turns for Coil 2. The mutual inductance between two helical coils can be calculated by Neumann's form as follows,

$$M = N_1 N_2 \mu \sqrt{ab} \left(\left(\frac{2}{k} - k \right) K(k) - \frac{2}{k} E(k) \right) \quad (2.7)$$

where

$$k^2 = \frac{4ab}{d^2 + (a+b)^2} \quad (2.8)$$

where a and b are radii for the two coils, and d is center to center distance between them. $K(k)$ and $E(k)$ are complete elliptic integrals of the first and second kind. Matlab function *ellipke* can compute the value of $K(k)$ and $E(k)$ for a given k . But another method is used in this thesis. BiotSavart Software is capable of calculating mutual inductance between two coils. The mutual inductance can be calculated by setting the current value in Coil 1 but zero in Coil 2. The linked flux in Coil 2 can be obtained by pressing Linked-flux button in Calc tab. The calculated M from Equation (2.6) for both coaxial and coplanar

coils is presented below.

The configurations of two coaxial coils are shown in Figure 2.9, where a and b indicate the radii for Coil 1 and 2. The center to center distance between them is d . The two coils have fixed radii of one inch ($a=b=2.54\text{cm}$). Coils are fabricated with 22 AWG wire. The pitch equals to wire diameter of 0.6452mm.

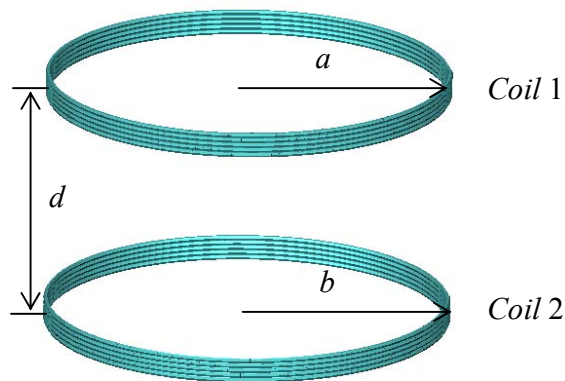


Figure 2.9 Configuration of coaxial coils

The relation between mutual inductance and distance for two coaxial coils are described in Figure 2.10. In this calculation, we can see that the mutual inductance decreased sharply as the gap d becomes larger. The value of mutual inductance M is roughly proportional to the inverse of distance. If we fix the center to center distance d between the two coils, the variations of mutual inductance as number of turns N are presented in Figure 2.11. As the number of turns becomes larger, the mutual inductance

almost goes up linearly.

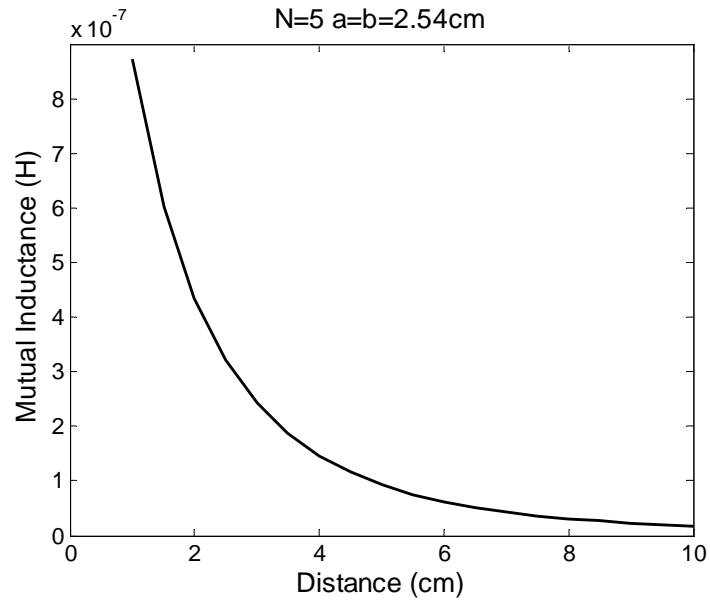


Figure 2.10 Mutual inductance vs. Distance for coaxial coils

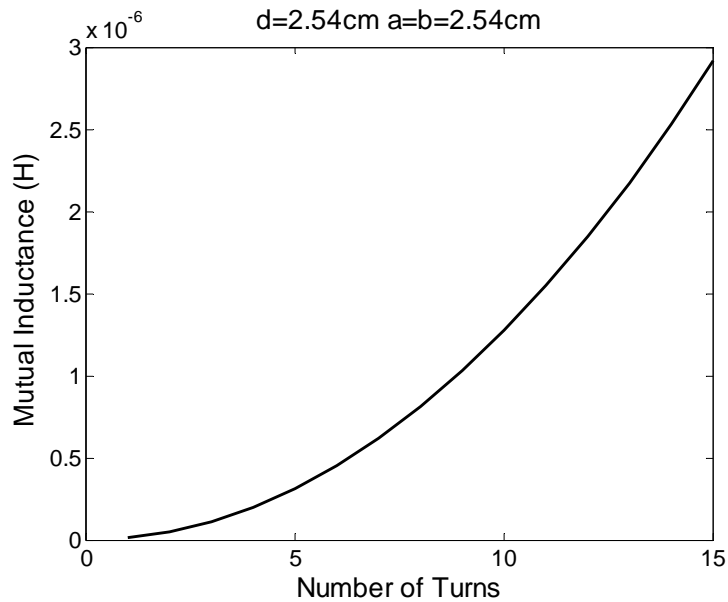


Figure 2.11 Mutual inductance vs. Number of turns for coaxial coils

Figure 2.12 presents the structure of two coplanar coils. The two coils have same radii of one inch ($a=b=2.54\text{cm}$). d is the gap between two coplanar coils, which is equivalent to subtracting coil diameter from center to center distance of two coils. The 22 AWG wires are used to winding coils. Mutual inductance for coplanar coils is negative since the angle between magnetic flux density \mathbf{B} in Coil 2 induced by the current I_1 and surface element ds are greater than 90 degrees, which makes M_{12} negative. From Figure 2.13, the absolute value of mutual inductance is still decreasing as Coil 2 goes further away from Coil 1, and rising when more turns is added, as shown in Figure 2.14.

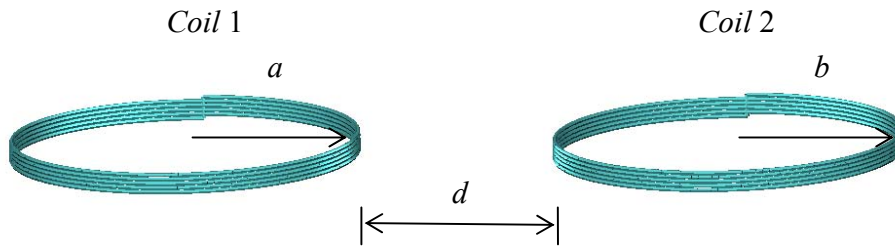


Figure 2.12 Configuration of coplanar coils

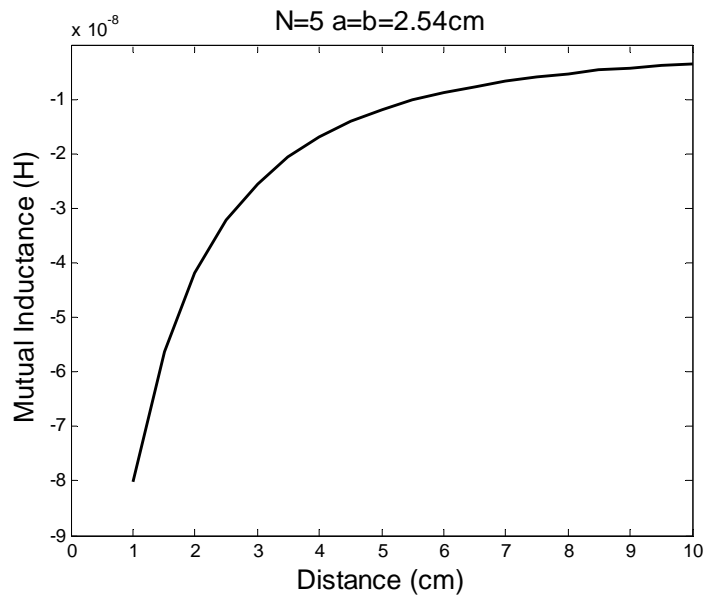


Figure 2.13 Mutual inductance vs. Distance for coplanar coils

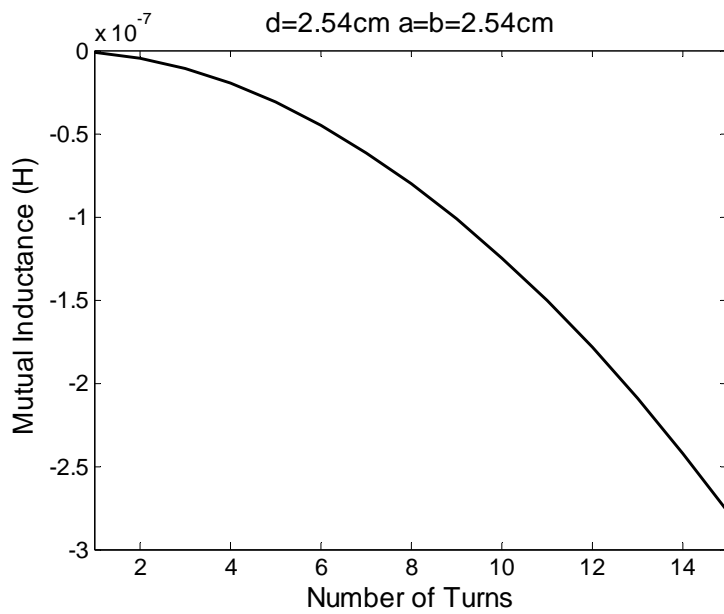


Figure 2.14 Mutual inductance vs. Number of turns for coplanar coils

2.3 1-D Corrosion Sensor Array

Passive wireless sensors can provide the most direct measurement of corrosion condition at a local point. For a civil infrastructure, the damage must be monitored to prolong the service lifespan and reduce the risk of major accidents. So there is a great demand to develop reliable, effective sensor systems to detect the corrosion within civil structure. The passive wireless sensor net can extend the coverage and abilities of individual sensors to monitor corrosion in a large scale.

2.3.1 Circuit Model

1-D linear sensor array is constructed using a number of coaxial inductively coupled corrosion sensors. Figure 2.9 and Figure 2.12 show the two options of sensor arrangement-coaxial and coplanar. In coaxial sensor net, corrosion sensors are spaced uniformly by distance d and the coil plane is perpendicular to the line connecting the center of loops. Within coplanar sensor net, all corrosion sensors are placed at the same plane and the gap between two nearest coils is distance d . The sensor array is excited by voltage at the driver coil. The current in the first loop induces current in the adjacent coil by magnetic linked flux, which induces further current in the same principle. This results in the magneto-inductive (MI) waves propagating along the sensor coils [25]. The coaxial and coplanar configurations can be simulated with the same equivalent circuit model, as shown in Figure 2.15.

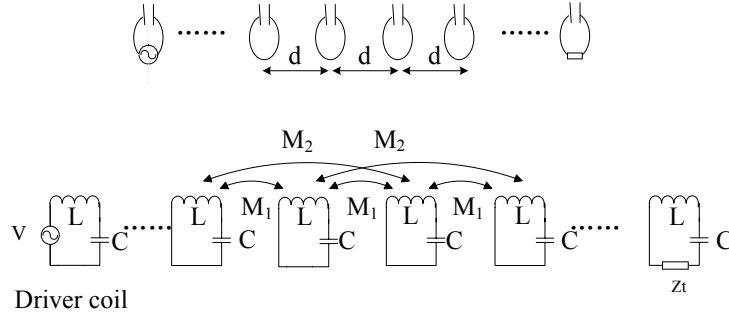


Figure 2.15 Schematic diagram and circuit model of passive wireless sensor array

In the magnetically coupled sensor array, every passive wireless sensor is modeled as a series circuit with components of inductance L_n , capacitance C_n and resistance R_n . Therefore self impedance Z_n for the n th sensor circuit is,

$$Z_n = R_n + j \left(\omega L_n - \frac{1}{\omega C_n} \right) \quad (2.9)$$

where ω is the angular frequency. Passive corrosion sensors used to build the sensor array are identical that make $R_n=R$, $L_n=L$ and $C_n=C$ ($n=1,2,\dots,N$). We define I_n and V_n as current and voltage in n th coil, and V_n is zero elsewhere except at driver coil. M_s indicates mutual inductance with the s th neighboring element. The current I_n will induce a voltage $j\omega M_{|n-m|}I_n$ in m th sensor loop by magnetic coupling, so I_m and V_m should satisfy,

$$V_m = Z_m I_m + \sum_{n \neq m} j\omega M_{|m-n|} I_n \quad (2.10)$$

Equation (2.10) can be written into matrix form as follows,

$$\begin{bmatrix}
Z_1 & j\omega M_1 & j\omega M_2 & \dots & & & & & & & \\
j\omega M_1 & Z_2 & j\omega M_1 & j\omega M_2 & \dots & & & & & & \\
j\omega M_2 & j\omega M_1 & Z_3 & j\omega M_1 & j\omega M_2 & \dots & & & & & \\
\dots & j\omega M_2 & j\omega M_1 & Z_4 & j\omega M_1 & j\omega M_2 & \dots & & & & \\
& \dots & j\omega M_2 & j\omega M_1 & Z_5 & j\omega M_1 & j\omega M_2 & \dots & & & \\
& & \dots & \ddots & \ddots & \ddots & \ddots & \ddots & \dots & & \\
& & & \dots & j\omega M_2 & j\omega M_1 & Z_{N-2} & j\omega M_1 & j\omega M_2 & & \\
& & & & \dots & j\omega M_2 & j\omega M_1 & Z_{N-1} & j\omega M_1 & & \\
& & & & & \dots & j\omega M_2 & j\omega M_1 & Z_N & &
\end{bmatrix}
\begin{bmatrix}
I_1 \\
I_2 \\
I_3 \\
I_4 \\
I_5 \\
\vdots \\
I_{N-2} \\
I_{N-1} \\
I_N
\end{bmatrix}
=
\begin{bmatrix}
V_1 \\
0 \\
0 \\
0 \\
0 \\
\vdots \\
0 \\
0 \\
0
\end{bmatrix}
\quad (2.11)$$

Equation (2.11) can be seen as the matrix form of Ohm's Law ($\mathbf{ZI}=\mathbf{V}$). The impedance matrix \mathbf{Z} is a $N \times N$ symmetrical matrix, while current \mathbf{I} and voltage \mathbf{V} are $N \times 1$ vectors. The main diagonal elements in impedance matrix are self impedance of n th ($n=1,2,\dots,N$) sensor circuit. The off diagonal expression $j\omega M_s$ are mutual impedance induced by another loop. From the matrix form, we can see that if electrical and configuration parameters (R, L, C, V_1 and M_s) of each passive wireless sensors are given, the current in elements of the sensor array can be solved as product of inverse impedance matrix and voltage, as expressed in Equation (2.12).

$$\begin{bmatrix} I_1 \\ I_2 \\ I_3 \\ I_4 \\ I_5 \\ \vdots \\ I_{N-2} \\ I_{N-1} \\ I_N \end{bmatrix} = \begin{bmatrix} Z_1 & j\omega M_1 & j\omega M_2 & \dots & & & & & & & \\ j\omega M_1 & Z_2 & j\omega M_1 & j\omega M_2 & \dots & & & & & & \\ j\omega M_2 & j\omega M_1 & Z_3 & j\omega M_1 & j\omega M_2 & \dots & & & & & \\ \dots & j\omega M_2 & j\omega M_1 & Z_4 & j\omega M_1 & j\omega M_2 & \dots & & & & \\ & \dots & j\omega M_2 & j\omega M_1 & Z_5 & j\omega M_1 & j\omega M_2 & \dots & & & \\ \vdots & & \dots & \ddots & \ddots & \ddots & \ddots & \ddots & \ddots & \dots & \\ \dots & & & \dots & j\omega M_2 & j\omega M_1 & Z_{N-2} & j\omega M_1 & j\omega M_2 & & \\ \dots & & & & \dots & j\omega M_2 & j\omega M_1 & Z_{N-1} & j\omega M_1 & & \\ \dots & & & & & \dots & j\omega M_2 & j\omega M_1 & Z_N & & \end{bmatrix}^{-1} \begin{bmatrix} V_1 \\ 0 \\ 0 \\ 0 \\ 0 \\ \vdots \\ 0 \\ 0 \\ 0 \end{bmatrix} \quad (2.12)$$

2.3.2 Dispersion Relationship

The coaxial and coplanar resonant sensor array is a form of embodiment of MI waveguide. The propagation of magneto-inductive (MI) waves is supported by the elements being coupled to other elements. The dispersion relationship can be calculated by considering the current distribution in all sensors. Considering a simple traveling wave solution $I_n = I_0 \exp(-nkd)$ for Equation (2.10), we obtain the dispersion relationship [26],

$$\omega^2 / \omega_0^2 - 1 - \frac{j}{Q} = \sum_{s=1}^S 2\kappa_s \cosh(skd) \quad (2.13)$$

where ω_0 is the resonant angular frequency of sensor circuit, $Q = \omega L / R$ is quality factor and $\kappa_s = M_s / L$ is coupling factor between two elements, $k = \alpha + j\beta$ is wave number and complex. The real part α and imaginary part β indicate the attenuation coefficient and propagation coefficient respectively. S is the maximum value of s . The magnetic coupling from all elements within the range of Sd (for coaxial) and $S(d+a+b)$ (for coplanar) will be considered.

To present the characteristics of dispersion relationship, the coils with five turns and radii of 2.54cm are used to build passive wireless sensor array as a MI waveguide. The measured self inductance of 5-turn coil winding by 22 AWG wire is 2.89×10^{-6} H. The resistance is calculated for a conductivity of 5.8×10^7 s/m is about 325.3m Ω . The additional capacitance is 101pF. For the n th element in coaxial sensor array with spacing d of one inch (2.54cm), the mutual inductances with its closest neighbors are $M_1 = 3.15 \times 10^{-7}$ H, $M_2 = 9.02 \times 10^{-8}$ H, $M_3 = 3.49 \times 10^{-8}$ H, $M_4 = 1.65 \times 10^{-8}$ H and $M_5 = 8.96 \times 10^{-9}$ H computed by BiotSavart Software. The center to center distance for the coplanar sensor net are chosen 6.08cm ($d=1$ cm), the first five mutual inductances are $M_1 = -8.02 \times 10^{-8}$ H, $M_2 = -6.34 \times 10^{-9}$ H, $M_3 = -1.77 \times 10^{-9}$ H, $M_4 = -7.31 \times 10^{-10}$ H and $M_5 = -3.71 \times 10^{-10}$ H. The dispersion relationship for coaxial and coplanar sensor array with $S=1$ and $S=5$ are presented in Figure 2.16 and Figure 2.17.

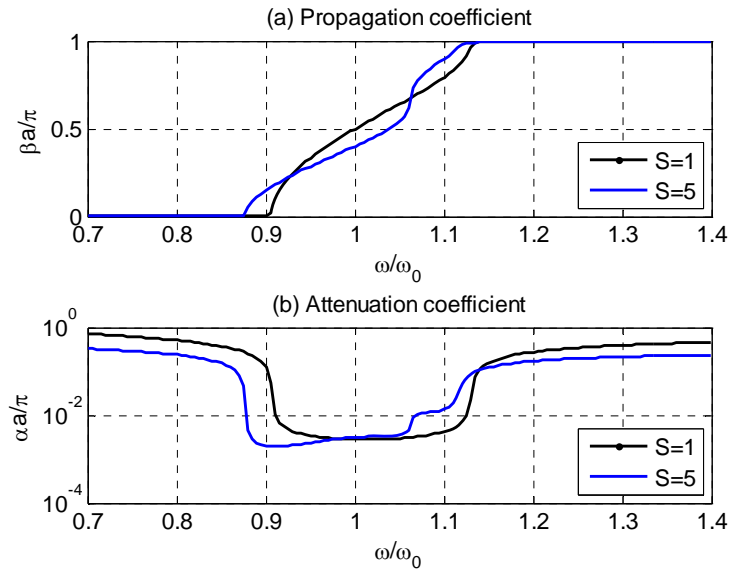


Figure 2.16 Dispersion relationship for coaxial sensor array with $d=2.54\text{cm}$

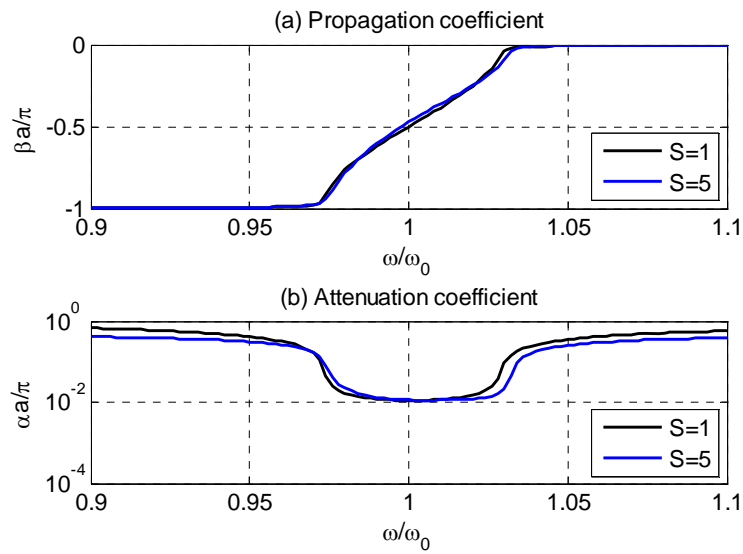


Figure 2.17 Dispersion relationship for coplanar sensor array with $d=1\text{cm}$

Both MI waveguides overall behave as bandpass filters from the two plots of attenuation coefficient above. The MI waves can travel along the passive wireless sensor

array around resonant frequency of sensor circuit. Comparing Figure 2.16 with Figure 2.17, coaxial sensor array has a wider passband and less minimum insertion loss than coplanar sensor array. This is because the coaxial sensor array here has stronger coupling than that of coplanar sensor array. Solid curve ($S=5$) and dash curve ($S=1$) for coaxial sensor array have greater difference than that of coplanar sensor array in simulation, since M_s ($s>1$) for coplanar arrangement are much more less than M_1 .

To simulate the propagation of MI waves along the linear sensor array, taking more interactions into account will provide more accurate results, which will increase the computational effort. The value of S depends on the variation of mutual inductance as distance between two elements is widened. From the analysis in section above, the magnitude of mutual inductance decreases sharply for both coaxial and coplanar coils. If M_1 is much greater than M_s ($s>1$), only taking the mutual coupling from nearest neighbor into consideration is a reasonable approximation. This can be seen in Figure 2.17, in which the ratio of M_2 to M_1 is 0.079 for coplanar sensor array ($d=1\text{cm}$). Equation (2.13) with only the nearest interaction is simplified as,

$$\omega^2/\omega_0^2 - 1 - \frac{j}{Q} = 2\kappa_1 \cosh(kd) \quad (2.14)$$

If we replace k with α and β , Equation (2.14) can be divided into two parts- real and imaginary part,

$$\omega^2/\omega_0^2 - 1 = 2\kappa_1 \cos(\beta d) \frac{\exp(\alpha d) + \exp(-\alpha d)}{2} \quad (2.15)$$

$$\frac{j}{Q} = 2j\kappa_1 \sin(\beta d) \frac{\exp(\alpha d) - \exp(-\alpha d)}{2} \quad (2.16)$$

The attenuation coefficient α is very small within the passband, so $\exp(\pm\alpha d)$ can be approximated as $1 \pm \alpha d$. Equation (2.15) and (2.16) are simplified as,

$$\omega^2/\omega_0^2 - 1 = 2\kappa_1 \cos(\beta d) \quad (2.17)$$

$$\frac{j}{Q} = 2j\kappa_1 \sin(\beta d) \alpha d \quad (2.18)$$

Equation (2.17) shows that MI waves can only propagate over the frequency range $1/(1+2\kappa_1) \leq (\omega/\omega_0)^2 \leq 1/(1-2\kappa_1)$, which depends on the coupling factor κ_1 . The lower frequency edge corresponds to $\beta d=0$, while the high frequency edge is reached at $\beta d=\pi$. Higher coupling factor κ_1 contributes to a wider passband.

From the analysis of mutual inductance above, we can get the coupling factor variations with distance, as shown in Figure 2.18. Higher coupling factor can be achieved by narrowing the gap between elements when the configurations of coils do not change. The corresponding passband widths are presented in Figure 2.19. Since the magnitude of coupling factor for coaxial sensor array is much greater than that for coplanar sensor array, the coaxial sensor array as MI waveguide has wider passband.

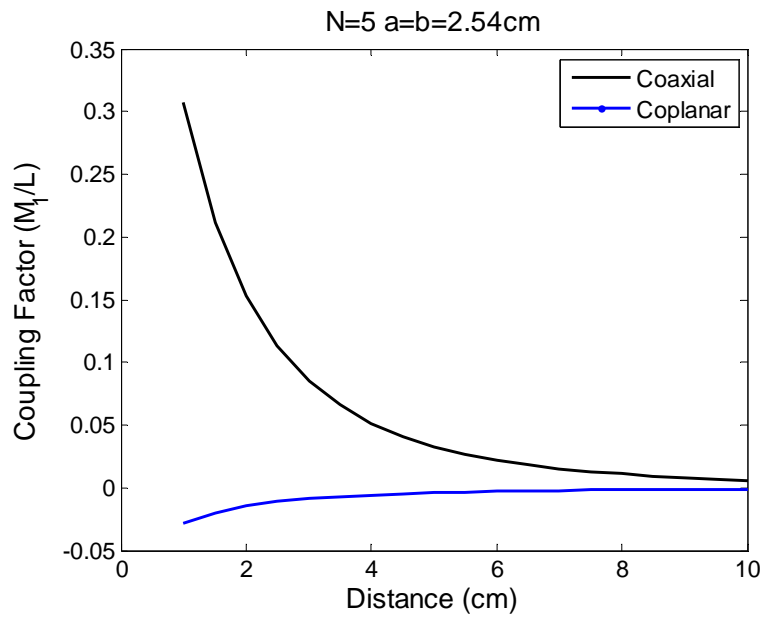


Figure 2.18 Coupling factor vs. Distance for coaxial and coplanar coils

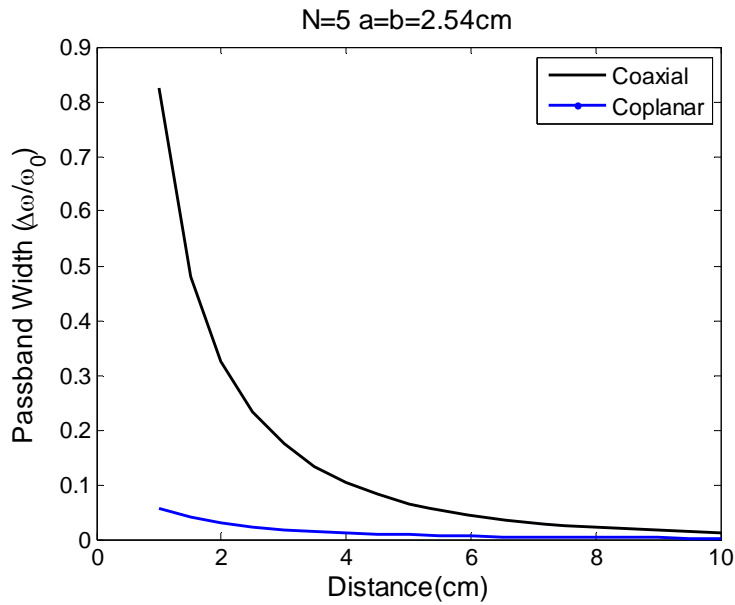


Figure 2.19 Passband width vs. Distance for coaxial and coplanar sensor arrays

Equation (2.18) shows that the attenuation coefficient α gets the minimum value $1/(\kappa_1 Qd)$ when βd equals $\pi/2$ at the mid band. The high-Q element and stronger coupling will help to decrease the minimum loss value.

2.3.3 Matched Impedance

As for an N -element sensor array, reflections will be introduced unless the transmission line terminated by its matched impedance. According to Equation (2.10), the current and voltage in last sensor loop obey,

$$Z_N I_N + j\omega M_1 (I_{N-1} + I_{N+1}) + j\omega M_2 (I_{N-2} + I_{N+2}) + \dots + j\omega M_S (I_{N-S} + I_{N+S}) = 0 \quad (2.19)$$

However, current I_{N+s} ($s=1,2,\dots,S$) are zero, then the traveling wave $I_n=I_0 \exp(-nkd)$ is not the solution of Equation (2.19). A matched impedance Z_t should be added to N th element to avoid end reflection,

$$(Z_N + Z_t) I_N + j\omega M_1 I_{N-1} + j\omega M_2 I_{N-2} + \dots + j\omega M_S I_{N-S} = 0 \quad (2.20)$$

where the matched impedance satisfy,

$$Z_t = j\omega M_1 \exp(-kd) + j\omega M_2 \exp(-2kd) + \dots + j\omega M_S \exp(-Skd) \quad (2.21)$$

The matched impedance varies as the frequency changes. Specific value of terminal impedance will only match the transmission line at one frequency and therefore provide matched termination at this specific frequency, but with increased loss at other frequencies.

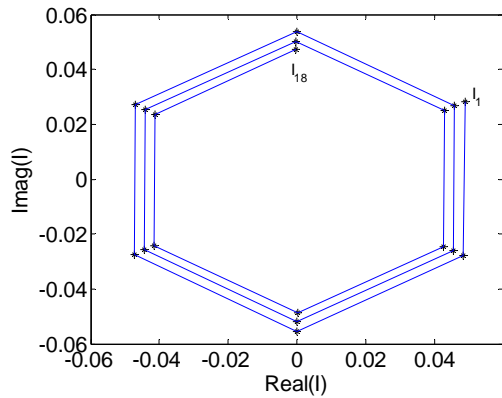
If we only take the nearest interaction into consideration, matched impedance Z_t equals to only one item $j\omega M_1 \exp(-kd)$. We list matched impedance at different frequencies in Table (2.2) and (2.3). At resonant frequency, the propagation coefficient βd equals to $\pi/2$ or $-\pi/2$ and matched impedance Z_t is purely resistive. It makes us easier to match the sensor array in experiment. For an 18-element sensor net terminated with matched impedance, the corresponding currents in each element are computed by Equation 2.12. Figure 2.20 plot the current distribution from 1st to 18th element for coaxial and coplanar sensor array. Since propagation coefficients βd of MI waves are both $\pi/3$, the phase shift per element is $\pi/3$ and the line linking value of currents make a hexagon. The vertexes are gradually converging to the center of hexagon due to attenuation which makes the absolute value of currents drop.

Table 2.2 Matched impedance at different frequency for coaxial sensor array

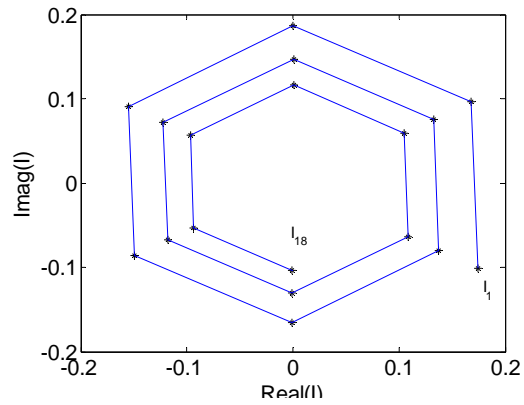
Normalized frequency	Propagation coefficient βd	Attenuation coefficient ad	Matched impedance Z_t
0.95	$\pi/3$	0.0034π	$14.99 + 8.66i$
1	$\pi/2$	0.0028π	18.26
1.06	$2\pi/3$	0.0031π	$16.74 - 9.67i$

Table 2.3 Matched impedance at different frequency for coplanar sensor array

Normalized frequency	Propagation coefficient βd	Attenuation coefficient αd	Matched impedance Z_t
1.01	$-\pi/3$	0.013π	$3.96 - 2.29i$
1	$-\pi/2$	0.011π	4.54
0.97	$-2\pi/3$	0.013π	$3.85 + 2.22i$



(a) Coaxial sensor array



(b) Coplanar sensor array

Figure 2.20 Current distribution for 18-element passive sensor array at $\beta d = \pi/3$

2.3.4 Insertion Loss

Insertion Loss is a measure of attenuation and defined as the loss of signal power resulting from the insertion of device. If the transmitted power is P_i and the power received by the load is P_o , the insertion loss in dB is given by

$$\text{Loss}=10\log_{10}\left(\frac{P_o}{P_i}\right) \quad (2.22)$$

The passive wireless sensor array is driven by the voltage in the first coil, and power is transmitted along the sensor array through the magnetic coupling between elements. The input power and output power can be expressed as [26],

$$P_i = \frac{1}{2} \text{Re}(I_1 V_1^*) \quad (2.23)$$

$$P_o = \frac{1}{2} |I_N|^2 \text{Re}(Z_t) \quad (2.24)$$

Substitute Equation (2.23) and (2.24) into Equation (2.22) of loss, we obtain,

$$\text{Loss}=10\log_{10}\left(\frac{\text{Re}(I_1 V_1^*)}{|I_N|^2 \text{Re}(Z_t)}\right) \quad (2.25)$$

With the calculation of current distribution and matched impedance, we can have the loss curve over a range of frequencies. The matched impedance is chosen as the value at resonant frequency. For the coaxial sensor array, the coil structure and parameters are the same as used in Section 2.3.2. The matched impedance Z_t is 18.2612Ω . Figure 2.21 presents insertion loss of coaxial sensor array with different number of elements.

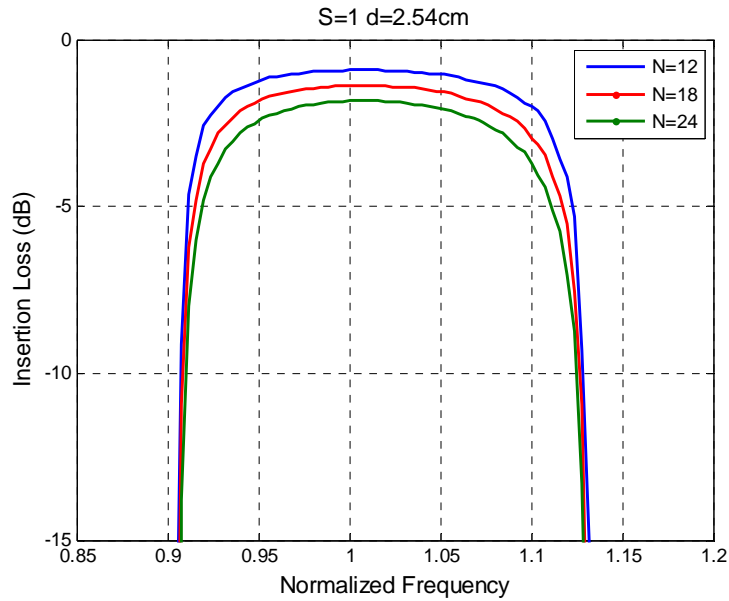


Figure 2.21 Insertion loss vs. Normalized frequency for coaxial sensor array with different number of elements

The frequency characteristics show passive wireless sensor array as MI waveguide act as a bandpass filter. MI waves can travel along the waveguide over the normalized frequency range ($0.91 < \omega/\omega_0 < 1.13$). As the passive wireless sensor array contains more elements, the minimum insertion losses go up gradually, while the passband width are almost the same. The coplanar sensor array constructed by the same coils is also investigated, which is terminated with matched impedance Z_t of 4.54Ω . The frequency characteristics are shown in Figure 2.22. Since the coplanar coils have weaker magnetic coupling than coaxial coils, minimum loss of the waveguide are greater and

passband width are much smaller. MI waves can only propagate along the coplanar sensor array within the normalized frequency range ($0.97 < \omega/\omega_0 < 1.03$).

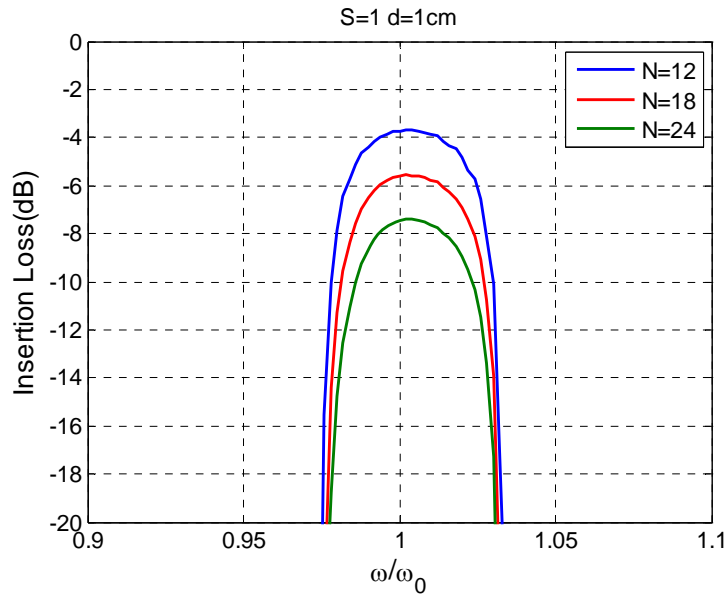


Figure 2.22 Insertion loss vs. Normalized frequency for coplanar sensor array with different number of elements

Figure 2.23 presents the frequency characteristics of coaxial sensor array with different spacing d , which is chosen as 2.54cm, 3.5cm and 4.5cm respectively. The corresponding matched impedances are 18.26Ω , 10.82Ω and 6.65Ω . The simulation is done with coaxial sensor array consisting of 18 identical 5-turn elements ended with matched impedance. We can see that wider distance have greater area coverage, but narrower passband width and larger minimum insertion loss. This is because the coupling

factor κ declines rapidly as the center to center distance d increase. The simulation results for coplanar sensor array are displayed in Figure 2.24. The matched impedances for $d=1\text{cm}$, 2cm and 3cm are 4.54Ω , 2.28Ω and 1.33Ω .

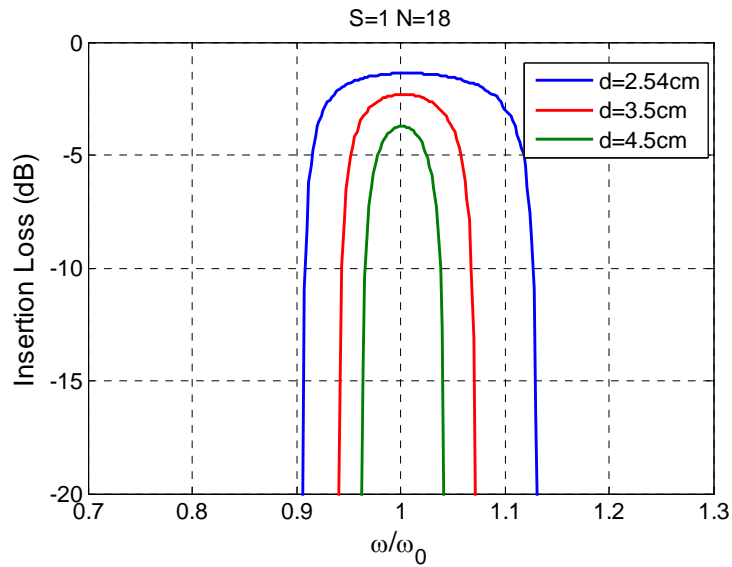


Figure 2.23 Insertion loss vs. Normalized frequency for coaxial sensor array with different axial spacing

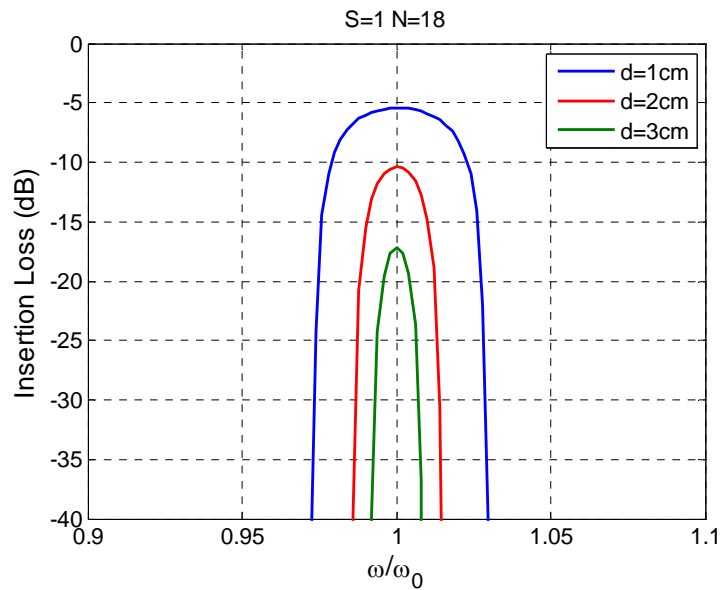


Figure 2.24 Insertion loss vs. Normalized frequency for coplanar sensor array with different gap

2.4 Summary

The embedded corrosion sensor with an exposed wire as a resistive transducer is an effective technique to provide corrosion information inside inaccessible concrete. To improve the ability and coverage of the corrosion sensors, 1-D linear corrosion sensor array are developed. The structure and corresponding circuit model are presented in this chapter. The linear array is driven by the voltage in the first sensor circuit and the energy is transmitted along the array by magnetic mutual coupling between elements. It shows that 1-D linear corrosion sensor array acts as a MI waveguide and its frequency characteristics are like a band pass filter. Furthermore, the frequency characteristics depend on both the configuration of point corrosion sensors and the distance between

them. High-Q element and stronger coupling contribute to wider passband and lower insertion loss. Coaxial sensor array have better performances than coplanar sensor arrangement with the same corrosion sensor elements.

CHAPTER 3 SENSING MECHANISM OF 1-D PASSIVE CORROSION SENSOR ARRAY

3.1 Introduction

The previous chapter has introduced the configuration and frequency characteristics of 1-D passive wireless sensor array constructed by magnetically coupled resonant sensors for detection of corrosion in concrete. The 1-D sensor array provides a greater coverage than point corrosion sensor. As previously stated, 1-D corrosion sensor array acts as a bandpass filter. The purpose of this chapter is to present the sensing mechanism of the sensor array that how to locate the corrosion in the line of sensors without interrogating the sensors individually.

3.2 1-D Corrosion Sensor Array with One Defect

1-D sensor array is constructed by a line of coupled passive wireless corrosion sensors spaced by distance d . At a local point, the onset of corrosion is detected by introducing the exposed wire in each sensor. The sensing wire is much smaller in diameter than the reinforcing bars, so the wire will break before structural damage occurred. The wire works as a switch to control the sensor circuit connected or not. A sensor circuit inside the array with broken wire makes the 1-D linear sensor array contain one defect.

3.2.1 Circuit Model

If the exposed wire of a sensor circuit is corroded through, the sensor circuit is open and decoupled with its neighbors. A mutual inductance variation is introduced by increasing the separation between two adjacent elements, as shown in Figure 3.1. This sensor does not contribute to transmitting energy and can be removed from the circuit model of intact array.

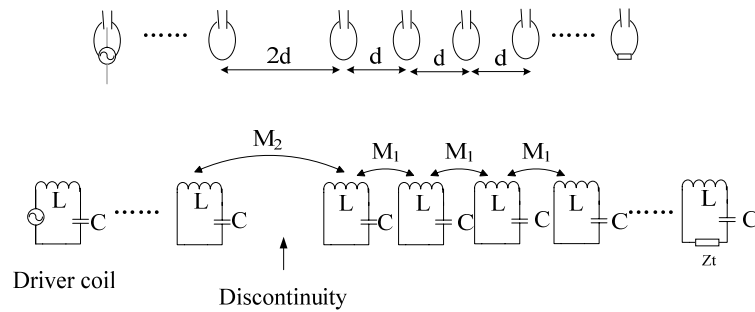


Figure 3.1 Schematic diagram and circuit model of 1-D sensor array with one defect

The n th sensor circuit with broken exposed wire carries no current. The energy is transmitted from $n-1$ th to $n+1$ th element directly through the mutual inductance M_2 . The sensor array can be considered as having $N-1$ th elements now. The embodiment of Ohm's law in the sensor array becomes,

shown in Figure 3.2, where I_i , I_r and I_t indicate the incident, reflective and transmitted wave caused by the impedance discontinuity.

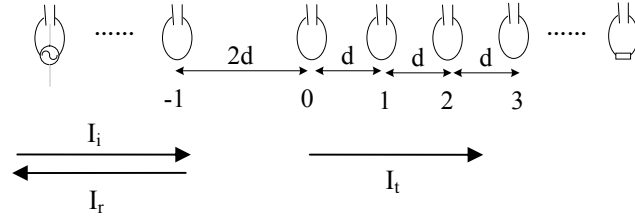


Figure 3.2 Schematic diagram of 1-D sensor array with one defect

The current in n th loop is described as [27],

$$I_n = \begin{cases} I_i + I_r = I \exp(-nkd) + RI \exp(nkd) & (n \leq -1) \\ I_t = TI \exp(-nkd) & (n \geq 0) \end{cases} \quad (3.3)$$

where R and T are the reflective coefficient and transmission coefficient. The current in the elements before the discontinuity junction is a combination of incident and reflective current. If only the magnetic coupling from the nearest neighbor is considered, the currents and voltages should satisfy,

$$\begin{aligned} ZI_{-1} + Z_1I_{-2} + Z_2I_0 &= 0 \\ ZI_0 + Z_1I_1 + Z_2I_{-1} &= 0 \\ ZI_1 + Z_1I_0 + Z_1I_2 &= 0 \end{aligned} \quad (3.4)$$

where Z_1 and Z_2 are mutual impedance, $Z_1=j\omega M_1$ and $Z_2=j\omega M_2$, then substitute Equation (3.3) into Equation (3.4), The equation set above can be simplified as,

$$\begin{aligned} Z_2(1+R) &= Z_1T \\ Z_1(\exp(kd) + R \exp(-kd)) &= Z_2T \exp(kd) \end{aligned} \quad (3.5)$$

The reflection coefficient R and transmission coefficient T are solved as,

$$R = \frac{(M_2^2 - M_1^2) \exp(kd)}{M_1^2 \exp(kd) - M_2^2 \exp(-kd)}$$

$$T = \frac{M_1 M_2 (\exp(kd) - \exp(-kd))}{M_1^2 \exp(kd) - M_2^2 \exp(-kd)}$$
(3.6)

Equation (3.6) shows that if M_2 do not equal to M_1 , reflection will take place. The strength of reflection depends on the ratio of Z_2 to Z_1 and value of kd . Since power is conserved, the two coefficients satisfy $|R|^2 + |T|^2 = 1$. $|R|^2$ and $|T|^2$ are power reflection and transmission coefficients. The relationship between two coefficients and M_2/M_1 at resonant frequency is presented in Figure 3.3. It shows that all energy will be transmitted when M_1 equals to M_2 . And the greater difference between the two mutual impedances, more energy will be reflected.

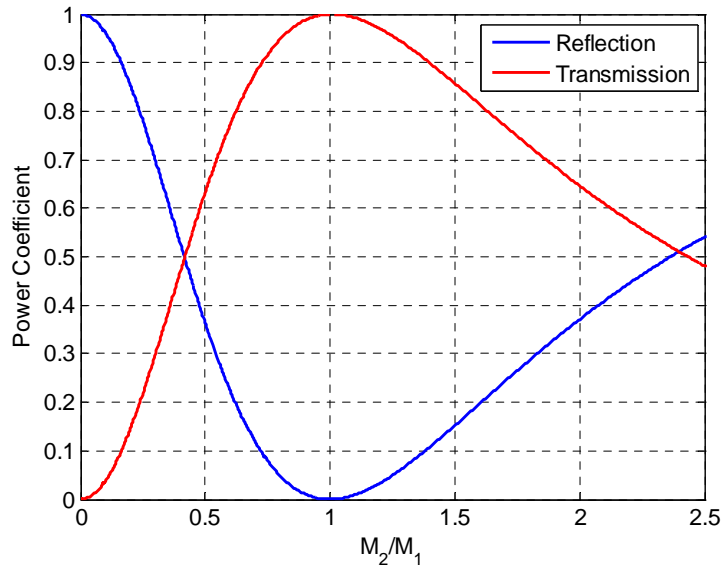


Figure 3.3 Power reflection and transmission coefficient vs. Mutual inductance ratio

The MI wave reflection also relates to the product of and spacing d and wave number k , which associate with frequency through the dispersion relationship. The

reflection and transmission coefficient variations as frequency for coaxial sensor frequency ($d=2.54\text{cm}$) are displayed in Figure 3.4. The reflection coefficients are much less than 1 within the passband ($0.9062 < \omega/\omega_0 < 1.1307$), and the curves vary slowly across the band. The transmission is high in the mid-band.

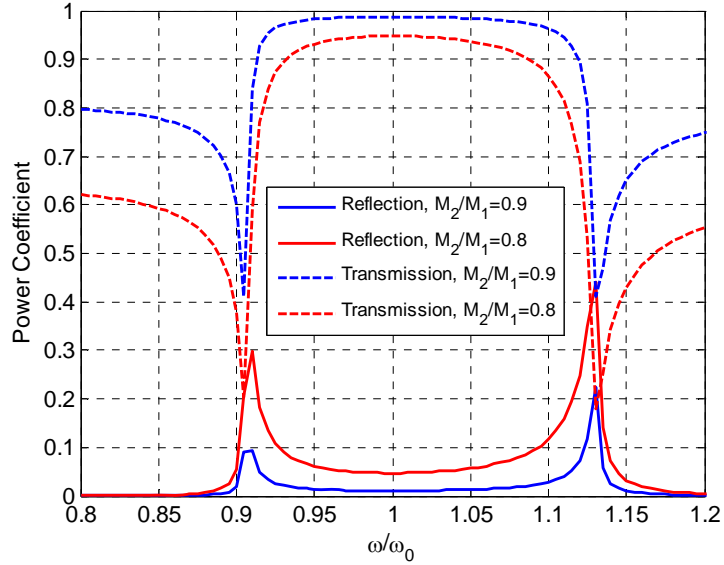


Figure 3.4 Power reflection and transmission coefficient vs. normalized frequency

If n th resonant sensor is corroded broken in the coplanar sensor array, the gap between $n-1$ th and $n+1$ th is $2d$ and the mutual inductance M_2 is $9.02 \times 10^{-8}\text{H}$ for 5-turn coil with diameter of one inch. The ratio of Z_2 to Z_1 is 0.29. Similarly, M_2 is 7.9 percent of M_1 for coplanar sensor array ($d=1\text{cm}$). The power reflection and transmission coefficient variations with ω/ω_0 for both sensor arrangements are presented below. It shows that the power transmission coefficient for coplanar sensor array is smaller than that for coaxial sensor array in the frequency band, since they have greater impedance difference.

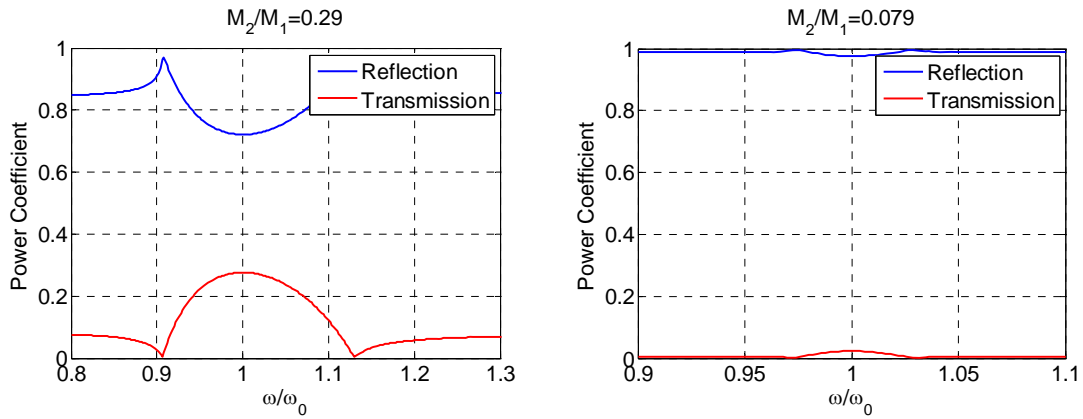


Figure 3.5 Power reflection and transmission coefficient vs. Normalized frequency for contact coaxial and coplanar sensor array

The insertion loss curve can also reflect how much the energy is transmitted in the waveguide. The simulation is done with the waveguide consisting of 5-turn corrosion sensors. Figure 3.6 shows the insertion loss for 12-element and 18-element sensor arrays with one defect. Data are provided over the MI wave frequency band. We can see that the magnetically coupled sensor array containing more elements with one defect has higher loss. The insertion loss increase as the defect sensor goes further away from the driver coil.

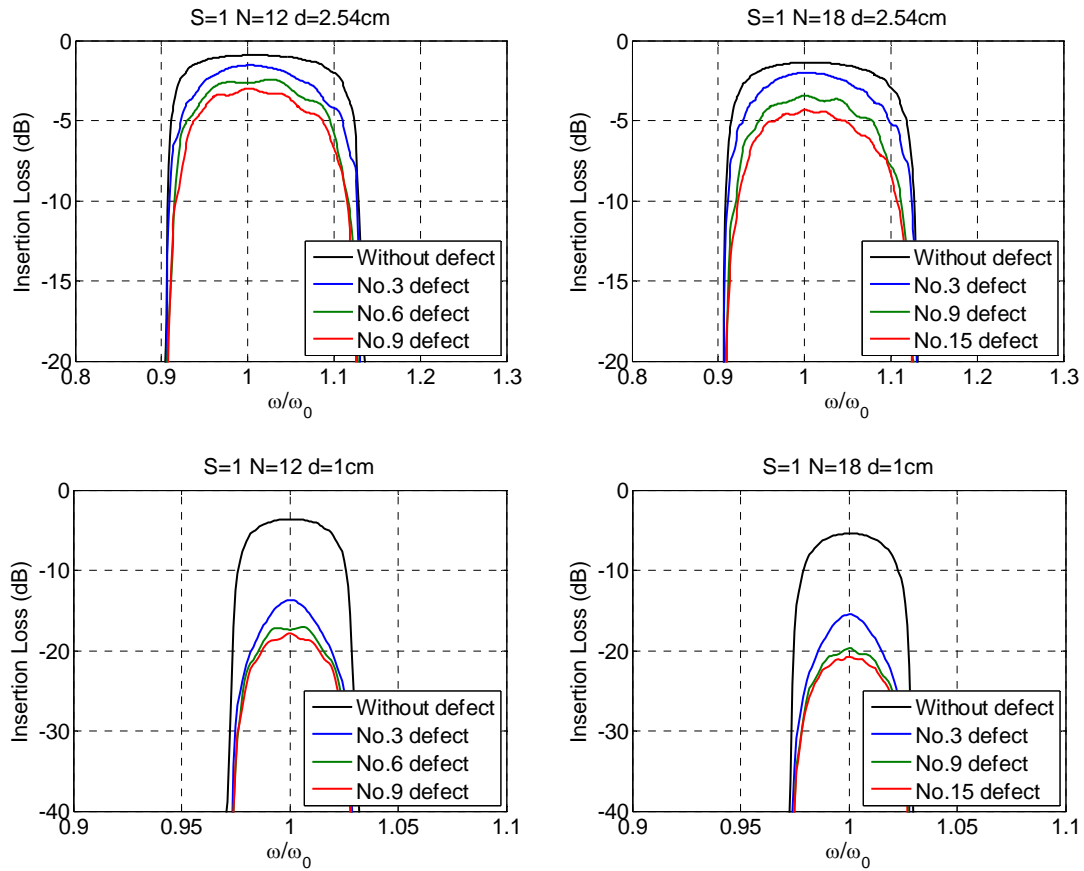


Figure 3.6 Insertion loss vs. Normalized frequency for coaxial and coplanar sensor array with one defect

From the analysis and results above, the defect will introduce more loss and small ripples during the passband. The extra loss by the defect is around 2dB for coaxial sensor array, while coplanar sensor array has additional 12dB in frequency band. And comparing the curves for different locations of defects, it is not easy for us to differentiate which sensor wire is broken. Although the coplanar provide more obvious difference, but the loss and width of frequency band are sacrificed. The little change of frequency characteristics provides a really low sensitivity to detect the corrosion. In experiment, this small difference would be offset by the noise.

3.3 1-D Corrosion Sensor Array with Two Defects

The onset of corrosion which corrodes exposed wire through will introduce mutual impedance discontinuity by widening the gap between elements. The frequency characteristics for 1-D sensor array with one discontinuity are similar to the perfect linear sensor array. The characteristics for linear sensor array with two defects will be further explored.

3.3.1 Circuit Model

1-D sensor array with two defects are classified into two different structures. If the second corrosion takes place next to the first discontinuity, it means a “mirror” with greater reflection will be introduced in the transmission line, as shown in Figure 3.7. This transmission line essentially only has one mutual inductance discontinuity with $Z_2=j\omega M_3$. The discontinuity impedance ratio M_3/M_1 is much small than M_2/M_1 , which would lead to a greater insertion loss in the frequency band.

The magnetically coupled sensor arrays are constructed by the same corrosion sensors as in previous section. For coaxial sensor array with spacing of 2.54cm, the ratio of M_3/M_1 and M_2/M_1 are 0.022 and 0.111 respectively. The loss variations with frequency are provided in Figure 3.8. It shows that the second corroded sensor that is adjacent to the first one introduces extra 5dB loss, which makes us much easier to detect the happening of corrosion. Also, data for coplanar sensor array having gap of 1cm is presented in Figure 3.9. Since M_3 is extremely small compared with M_1 for this sensor arrangement, the insertion loss goes to approximately -50 dB in the passband.

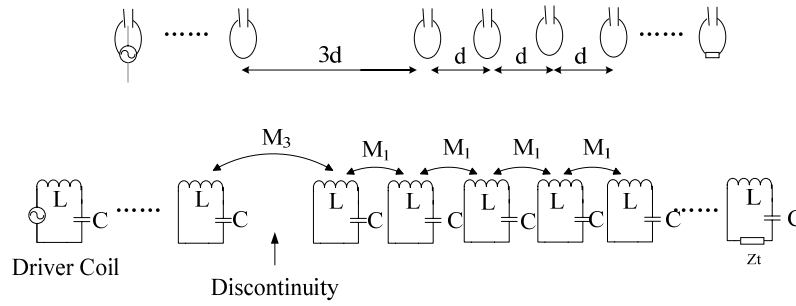


Figure 3.7 Schematic diagram and circuit model of 1-D sensor array with two adjacent defects

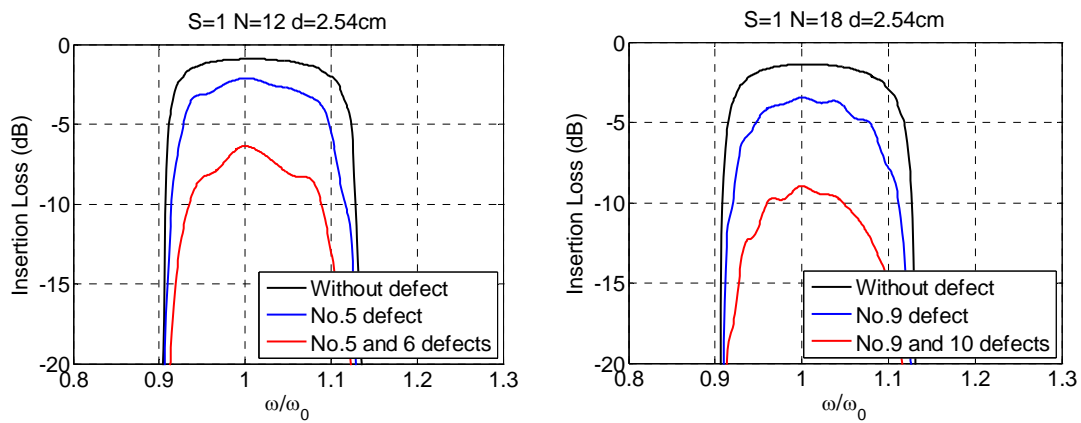


Figure 3.8 Insertion loss vs. Normalized frequency for coaxial sensor array with different number of elements

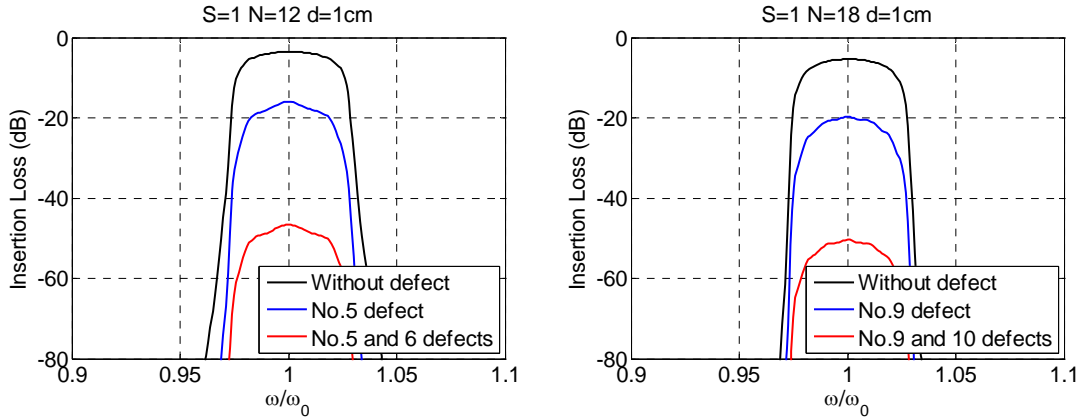


Figure 3.9 Insertion loss vs. Normalized frequency for coplanar sensor array with different defects

If the second corrosion happens at another location rather than the sensors nearby, two mutual inductance discontinuities will be formed in the line of corrosion sensors. The equivalent circuit model is shown in Figure 3.10, which is like two “mirrors” are plugged into the waveguide.

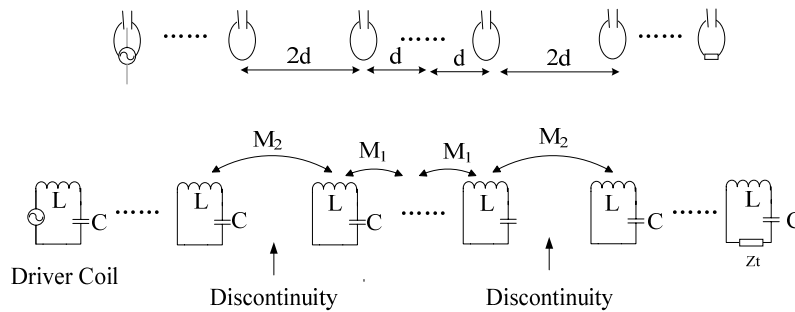


Figure 3.10 Schematic diagram and circuit model of 1-D sensor array with two distributed defects

If n_1 th and n_2 th sensor circuit are broken due to corrosion in N -element sensor array, both sensors will lose coupling with other elements. The embodiment of Ohm’s law

3.3.2 Frequency Characteristics

The frequency characteristics for 1-D sensor array with two neighboring defects have been investigated in the previous section. Two distributed defects will give rise to two reflections in the transmission line, as shown in Figure 3.11. The two mirrors act as a Fabry-Perot cavity [27]. The two reflectors divide the transmission line into three parts, and the current in each part can be described as in Equation 3.9.

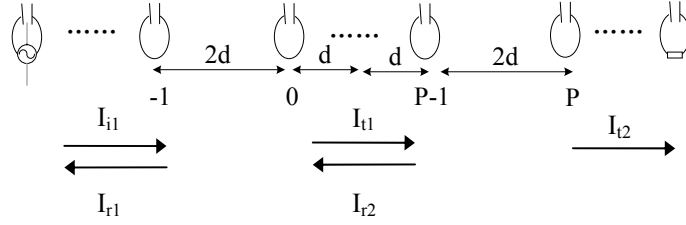


Figure 3.11 Schematic diagram of 1-D sensor array with two distributed defects

$$I_n = \begin{cases} I_{i1} + I_{r1} = I \exp(-nkd) + R_1 I \exp(nkd) & (n \leq -1) \\ I_{t1} + I_{r2} = T_1 I \exp(-nkd) + R_2 I \exp(nkd) & (0 \leq n \leq P-1) \\ I_{t2} = T_2 I \exp(-nkd) & (n \geq P) \end{cases} \quad (3.9)$$

where R_1 and R_2 indicate the coefficients of backward waves for loop n ($n \leq -1$ and $0 \leq n \leq P-1$), T_1 and T_2 are coefficients of forward waves for loop n ($0 \leq n \leq P-1$ and $n \geq P$). We assume the two discontinuities have the same mutual inductance Z_2 . The sensor circuits at the two junctions should satisfy,

$$\begin{aligned} ZI_{-1} + Z_1 I_{-2} + Z_2 I_0 &= 0 \\ ZI_0 + Z_1 I_1 + Z_2 I_{-1} &= 0 \\ ZI_{P-1} + Z_1 I_{P-2} + Z_2 I_P &= 0 \\ ZI_P + Z_1 I_{P+1} + Z_2 I_{P-1} &= 0 \end{aligned} \quad (3.10)$$

where P equals to the number of sensor working between the two discontinuities. We substitute current expression into Equation 3.10 and eliminate Z , R_2 and T_1 . The equation set can be simplified as follows,

$$\begin{aligned} T_2 (Z_1^2 - Z_2^2) \exp(-(2P-1)kd) - R_1 (Z_2^2 (\exp(-kd) - \exp(kd))) &= \exp(kd) (Z_2^2 - Z_1^2) \\ T_2 (Z_2^2 (\exp(-kd) - \exp(kd))) - R_1 \exp(-kd) (Z_1^2 - Z_2^2) &= Z_1^2 \exp(-kd) - Z_2^2 \exp(kd) \end{aligned} \quad (3. 11)$$

Reflection coefficient R_1 and transmission coefficient T_2 caused by the cavity are solved as,

$$\begin{aligned} R_1 &= \frac{(M_2^2 - M_1^2)(M_2^2 - M_1^2 \exp(2kd) - \exp(-2Pkd)(M_2^2 \exp(2kd) - M_1^2))}{(M_2^2 \exp(-kd) - M_1^2 \exp(kd)) - (M_1^2 - M_2^2) \exp(-2Pkd)} \\ T_2 &= \frac{M_1^2 M_2^2 (2 - \exp(2kd) - \exp(-2kd))}{(M_2^2 \exp(-kd) - M_1^2 \exp(kd)) - (M_1^2 - M_2^2) \exp(-2Pkd)} \end{aligned} \quad (3. 12)$$

Both coefficients depend on the mutual inductance M_1 and M_2 , the number of perfect sensors inside the resonator P , and wave number k . We plot the reflection coefficient $|R|^2$ and transmission $|T|^2$ variations with normalized frequency for coaxial and coplanar sensor arrays consisting of the same elements as described in Section 3.2. Figure 3.12 display the data in the frequency band for different defects in coaxial sensor array ($d=2.54\text{cm}$).

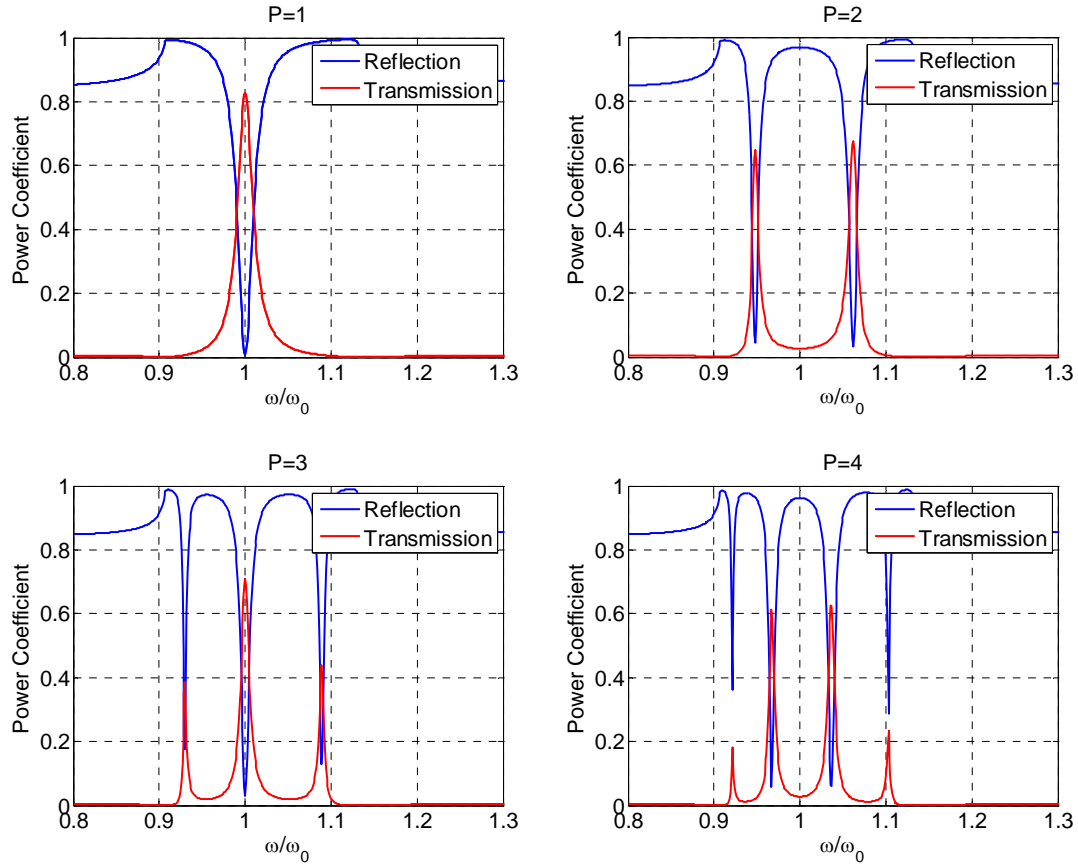


Figure 3.12 Power reflection and transmission coefficient vs. Normalized frequency for coaxial sensor array with two discontinuities

The transmitted power has a peak at the resonant frequency when P equals to 1. And when two sensors exist between the discontinuities, the peaks for transmission coefficient happen at normalized frequency of 0.95 and 1.06. Similarly, the power transmission coefficients have peak value at normalized frequency of 0.93, 1 and 1.09 when P reaches 3. The four peaks at 0.92, 0.97, 1.04 and 1.10 for transmission coefficient curve can be seen in the last plot in Figure 3.12. The addition of sensors produces larger number of transmission peaks. If the cavity contains P sensors, the peaks lie at frequency such that $\beta d = n\pi/(P+1)$, where $n=1,2,\dots,P$. This is the conventional cavity resonance

principle that resonance occur when the phase change $2(P+1)\beta d$ accumulated in a cavity round trip as a whole number of multiples of 2π [27].

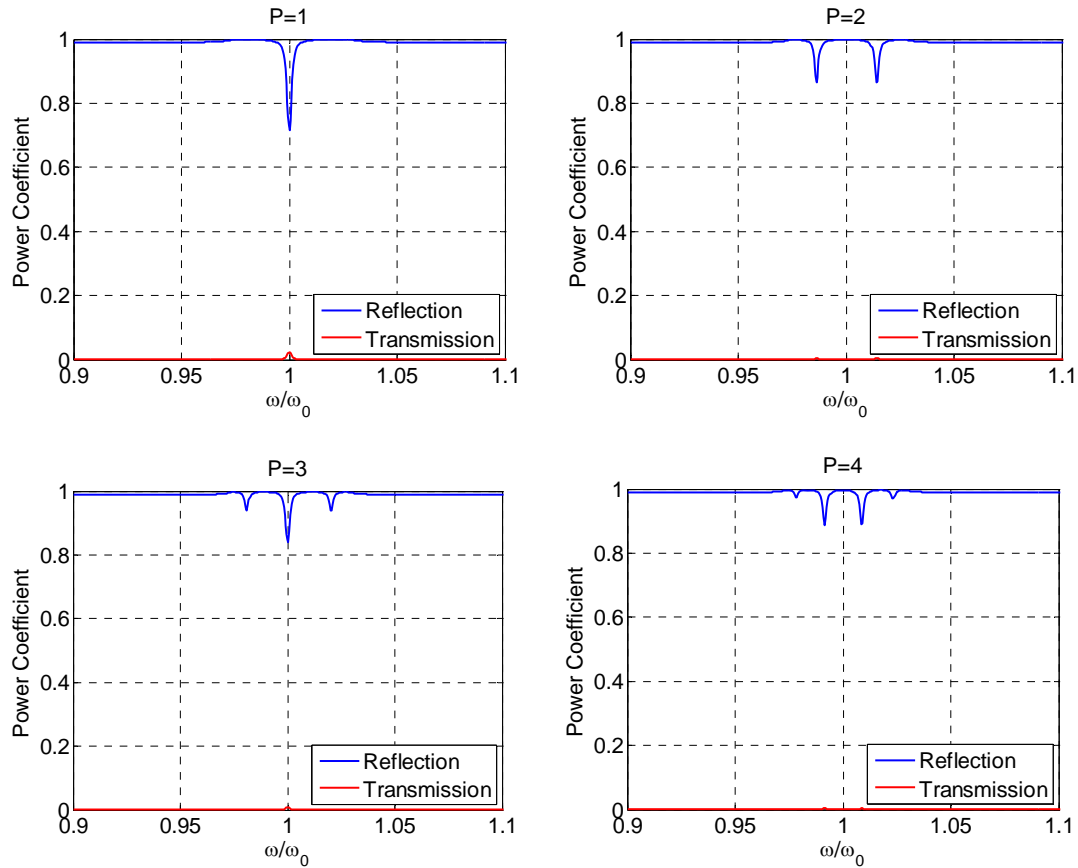


Figure 3.13 Power reflection and transmission coefficient vs. Normalized frequency for coplanar sensor array with two discontinuities

Figure 3.13 presents the coefficient data for coplanar sensor array ($d=1\text{cm}$) with two discontinuities. It should have the same characteristics of resonant peak as that of coaxial sensor array. However, the magnetic coupling between two adjacent coils after one sensor circuit is corroded through is so small that most energy can't be coupled to the next one and are reflected. But we can still see the corresponding notches in the reflection

coefficient curves.

In addition to the strength of magnetic coupling, the quality factor of coils also influences the power transmission. Figure 3.14 plot the coefficients variations with frequency for different quality factors at resonant frequency. It shows that peak for transmission coefficient is attenuated when quality factor decrease. More energy is consumed by the increased resistance, but the frequency where peaks lie at did not change.

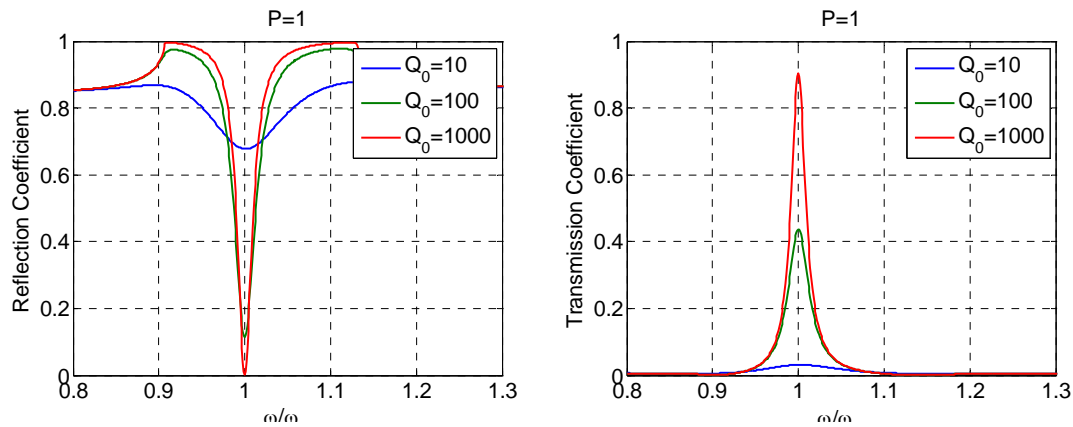


Figure 3.14 Power reflection and transmission coefficient vs. Normalized frequency with different quality factors at resonant frequency

The resonant peaks also happen at the insertion loss curve in the passband. The frequency that the peaks take place is in agreement with the location of peaks in the transmission coefficient curve. Figure 3.15 presents the insertion loss curve for 12-element coaxial sensor array with different locations of defects. We can see that the number of sensors P between two defects decides the number of peaks in the passband. For different sets of two defects, the location of peaks and troughs are identical for the same value of P . If the two defects are further away from the driver coil, the loss

difference between peaks and troughs will be larger, as shown in Figure 3.15. Figure 3.16 presents data for 12-element coplanar sensor array. The peaks have almost extra 20dB insertion loss and show a great difference in the passband characteristics.

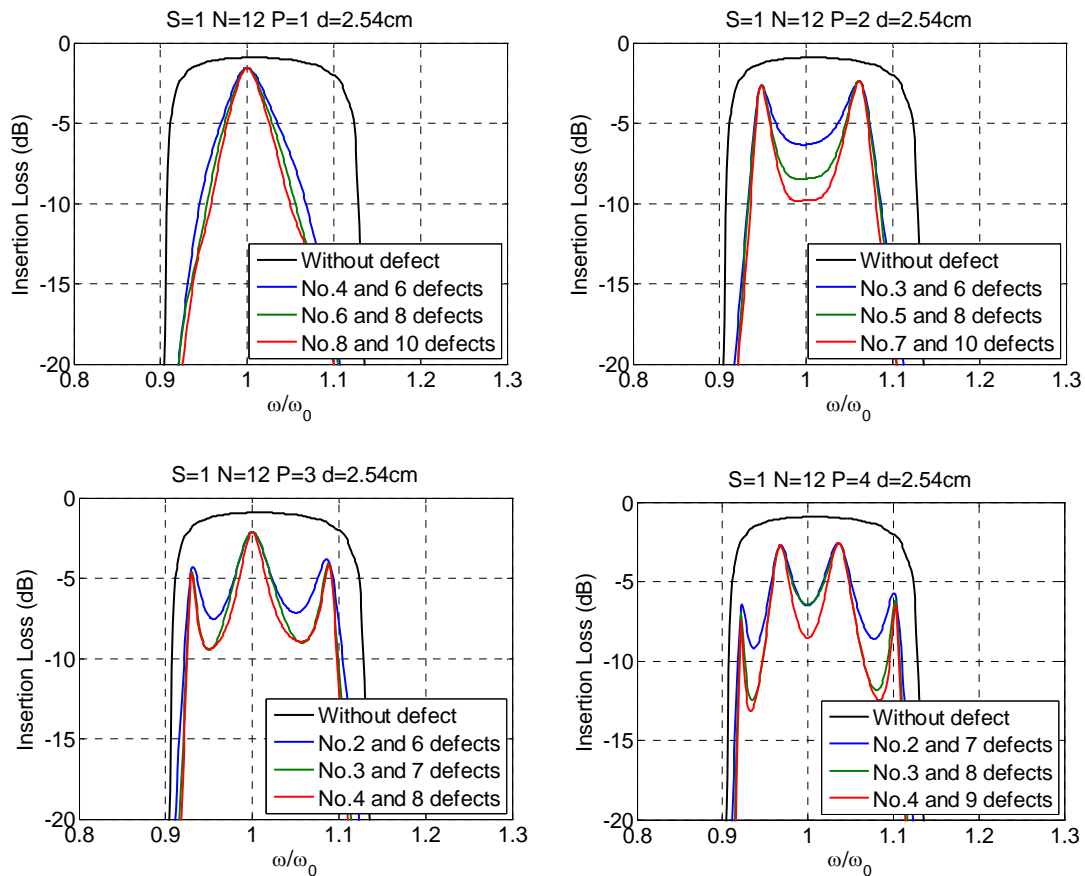


Figure 3.15 Insertion loss vs. Normalized frequency for coaxial sensor array with two discontinuities

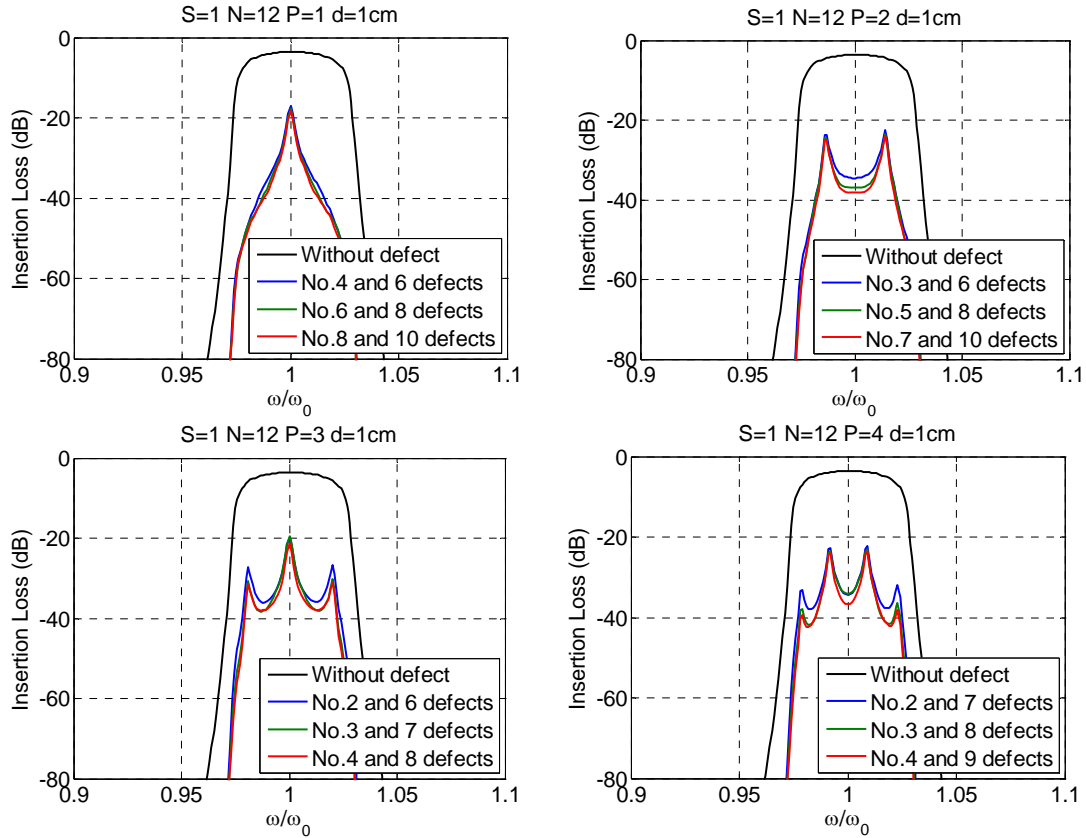


Figure 3.16 Insertion loss vs. Normalized frequency for coplanar sensor array with two discontinuities

3.4 Sensing Mechanism

In an inductively coupled sensor array, each sensor contains a steel sensing wire to detect the onset of corrosion. The corrosion of the external wire opens the circuit. From the transmission line theory, the introduced impedance discontinuity would give rise to wave reflection in the waveguide. The defect increases loss in passband and introduce some ripples due to mutual inductance discontinuity. The discontinuity in the transmission line acts as a mirror and the reflection varies slowly in the MI wave passband. However it is not obvious for us to detect the changes, since the curve shape is

similar and the loss gap between is small. It is hard to tell exactly which sensor is corroded broken.

If a second sensing wire is open, the two defects act as a Fabry-Perot cavity with P sensors. The resonant peaks happen at frequencies such that $\beta d = n\pi/(P+1)$, where $n=1,2,\dots,P$. To observe the presence of corrosion and locate the defect precisely, we intentionally set a defect as reference reflector in the 1-D passive sensor array.

We prefer to choose the second or the second-to-last element. For any group of two defects in the transmission line, if same number of intact sensors exists between, the number and location of peaks would be same. For example, if 6th sensor is set as the reference reflector, another defect at 3rd or 9th sensor will both make the loss curve containing two peaks, as shown in Figure 3.17. The two curves have the same peaks and corresponding frequency value. This would lead to two answers for the location of the corrosion. Although the dip for the 6th and 9th defects is deeper, it would be arbitrary to differentiate the two conditions by the height of dip since noise would disturb the dip in practical experiment. To guarantee the uniqueness of the frequency response, the second and the second-to-last elements could be chosen as the reference reflector. Any two defects combination would have unique frequency characteristics. Therefore, the onset of corrosion in the wire is a measure of the onset of corrosion in the reinforcement within an inductively coupled sensor array.

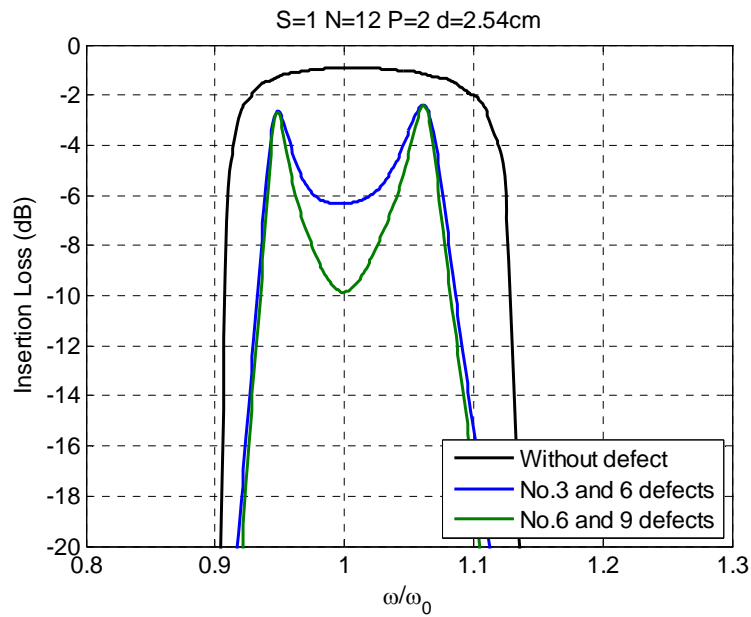


Figure 3.17 Insertion loss vs. Normalized frequency for coaxial sensor array with two discontinuities

The frequency characteristics of the sensor array with the second or the second-to-last elements as reference reflector are presented in Figure 3.18. The plots for both coaxial and coplanar 12-element sensor arrangement show that the sensor array with second defect has better performance. So we make the second sensor circuit open intentionally as the reference reflector.

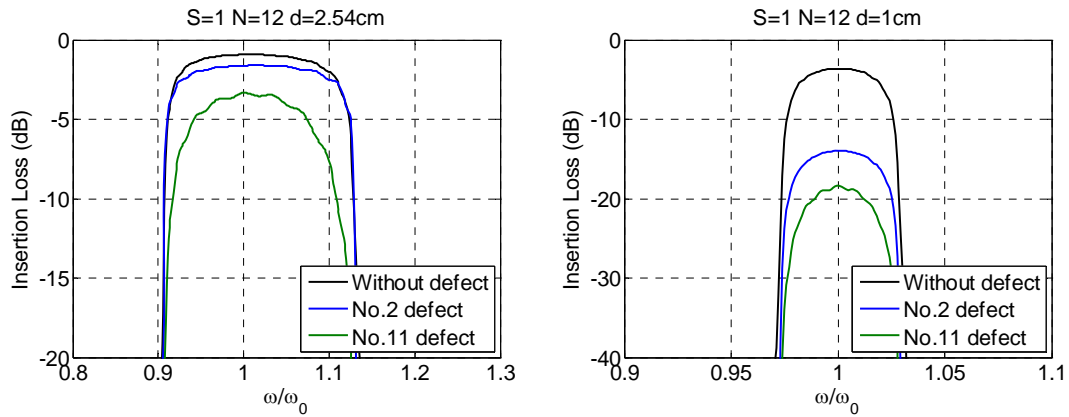


Figure 3.18 Insertion loss vs. Normalized frequency with the second or second-to-last element as reference reflector

Figure 3.19 and 3.20 show the data for coaxial and coplanar 12-element sensor arrays with different corrosion location, which accord with the analysis above. When the exposed wire in another sensor is corroded through, the second discontinuity is introduced. The resonant peaks will happen during the passband according to the location of the second discontinuity. The number of peaks depends on value of P and location of peaks can be expected by cavity resonance principle. The change of passband characteristics makes us much easier to detect the onset of corrosion at any location.

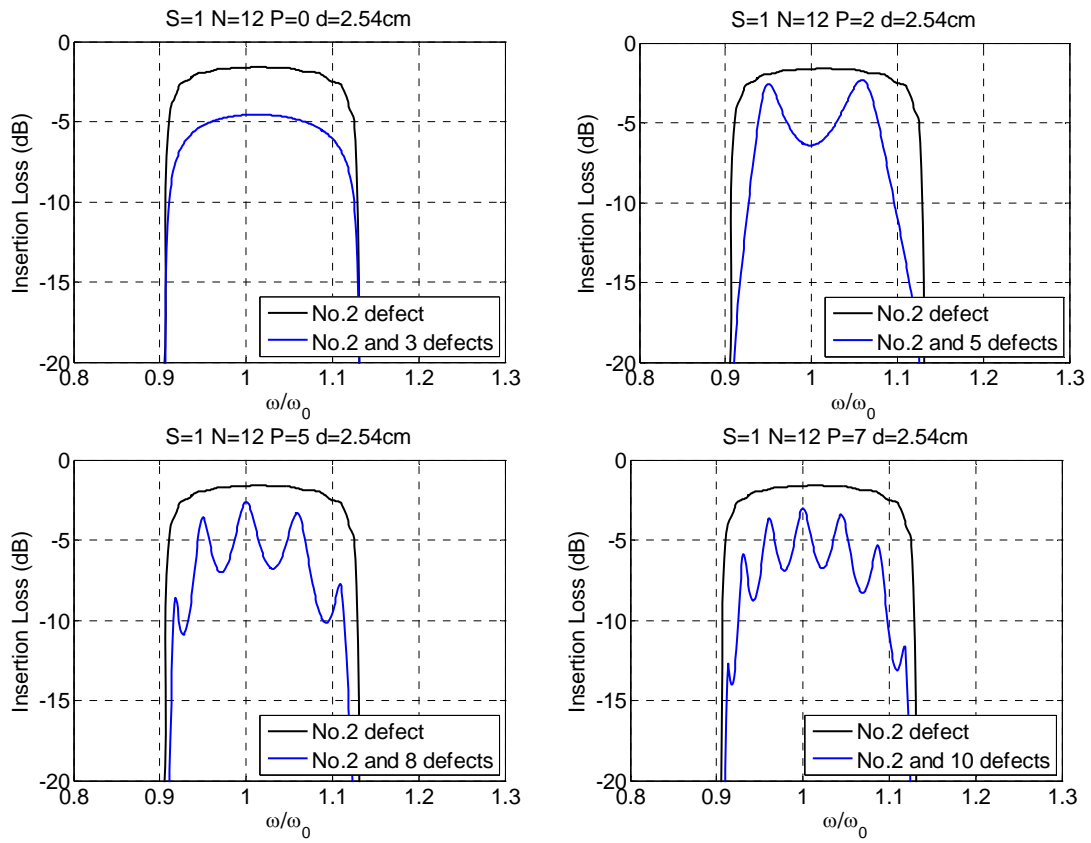


Figure 3.19 Insertion loss vs. Normalized frequency for coaxial sensor array with second corrosion sensor as reference reflector

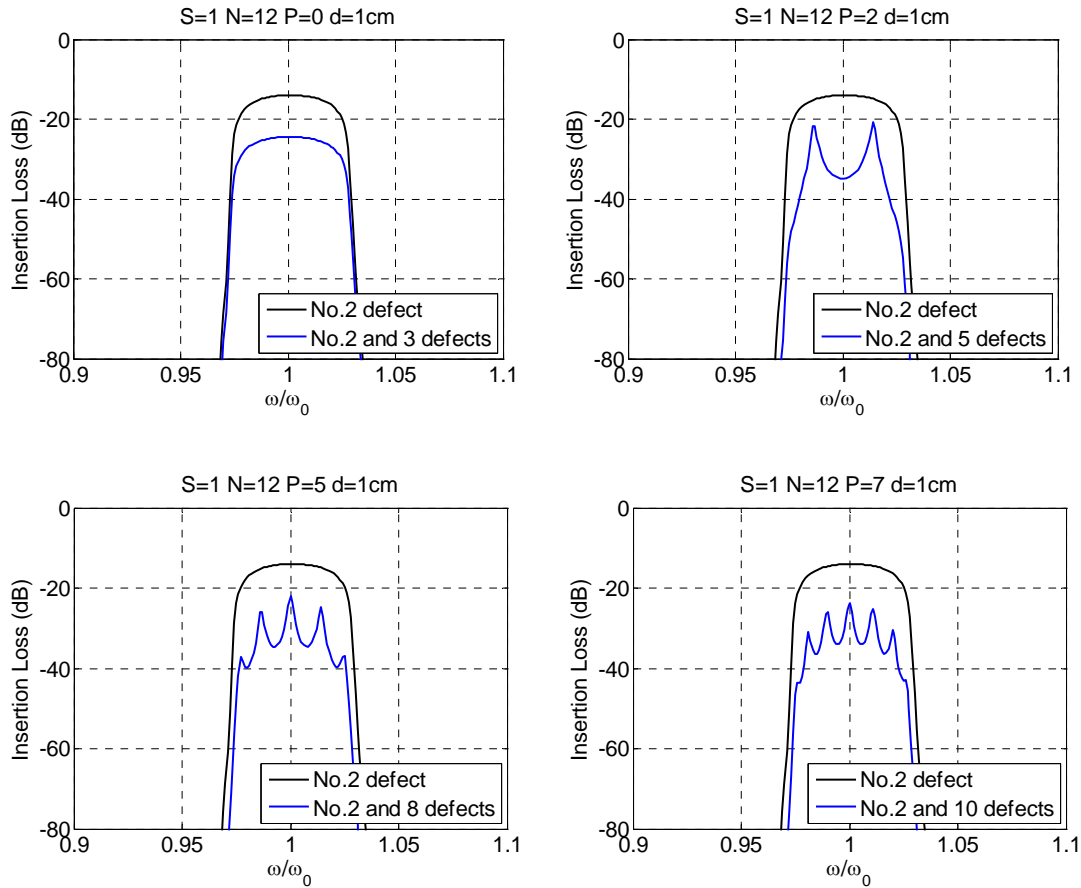


Figure 3.20 Insertion loss vs. Normalized frequency for coplanar sensor array with second corrosion sensor as reference reflector

3.5 Summary

1-D linear magnetically coupled sensor array extend the surveillance scale as distributed uncoupled sensors do. To get the local corrosion information, uncoupled corrosion sensors must be interrogated individually. In this chapter, we make use of the frequency characteristics of 1-D magnetically coupled sensor array as MI waveguide to locate the location exactly.

1-D linear sensor arrays with one defect are studied first. The wave reflection

and transmission coefficients are deduced from the equivalent circuit model. It shows that greater impedance difference and low quality factor give rise to greater reflection. The insertion loss as a waveguide increase after a defect is investigated. When the defect is go further away from the driver coil, the insertion loss will go up in the passband. For different locations of corroded sensors, the passband characteristics did not change so much that make us easy to differentiate.

The waveguide with two defects will form a Fabry-Perot resonant cavity. Resonant peaks will take place during the passband. The number of peaks depends on how many intact sensors exist in the cavity. This principle makes us easily to detect the onset of corrosion. So we set a sensor with broken wire intentionally as a reference reflector, and locate the happening of corrosion by counting the peaks during the passband. It provides a convenient and precise way to detect and locate corrosion. There is no need to test each sensor one by one.

CHAPTER 4 EXPERIMENTAL RESULTS IN THE AIR

4.1 Introduction

The purpose of this chapter is to present experimental results for developed passive wireless corrosion sensor arrays. Prior to embedding the sensors in a reinforced concrete member, the frequency characteristics were determined by interrogating the sensor array in air. In the experiment the exposed wire is not added to each sensor. We simulate the onset of corrosion by cutting off the circuit directly. These results are also summarized.

4.2 Basic Set Up

The point sensor is constructed from one inductor, one capacitor and one external switch as transducer. The coil is formed by wrapping an enamel coated 22AWG wire around a 2-inch plastic ring five times. The added capacitance is 101pF. The measured self inductance is about 2.89 μ H. All tags used in the coil chain have resonant frequency in the range 9.315MHz \pm 0.05MHz. The quality factor of each coil is around 115 based on their impedance characteristics as shown in Figure 4.1[28].

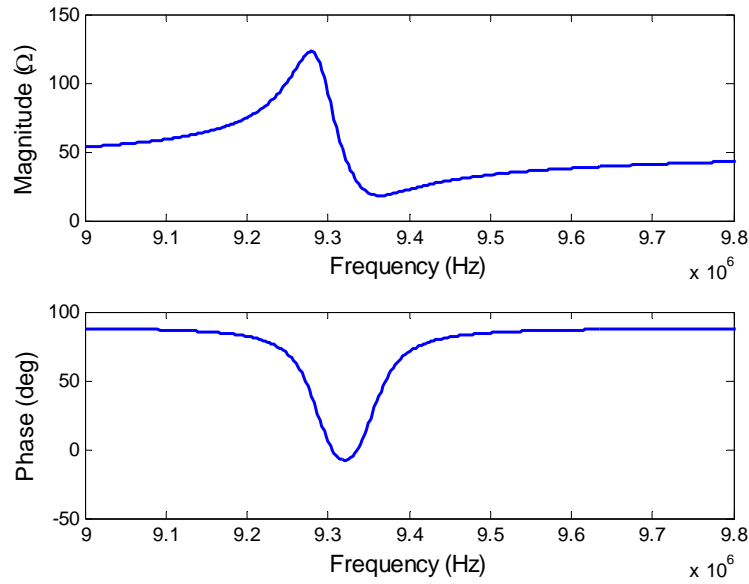


Figure 4.1 Magnitude and phase of sensor coil input impedance

The 1-D sensor array is built with a line of resonant passive sensors with driver and reader coils. The driver coil is used to provide a source of power. MI waves will propagate along the sensor array. With our analysis in previous chapter, coaxial sensor array has low loss due to stronger coupling. To build a low-loss MI waveguide, we place the passive sensors coaxially. They are uniformly spaced, as shown in Figure 4.2. The driver and reader coil both have the same structure except that the reader coil has matched impedance.

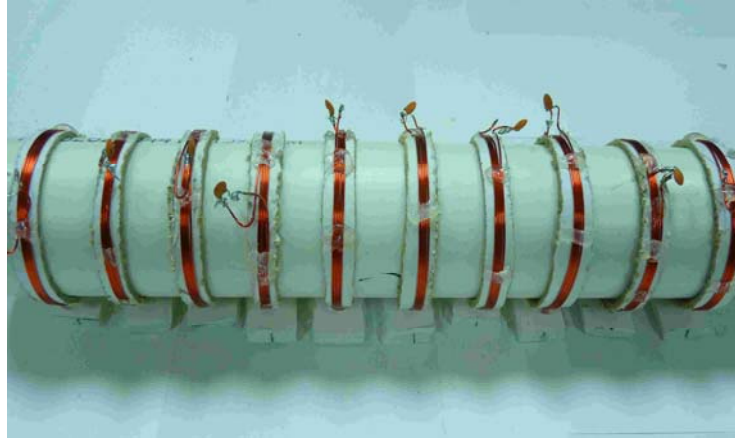


Figure 4.2 1-D magnetically coupled passive wireless sensors as MI waveguides

4.3 Test of 1-D Corrosion Sensor Array

4.3.1 Test of Intact 1-D Corrosion Sensor Array

The 1-D inductively coupled sensor array act as a MI waveguide. We first measure the frequency responses of our design of coaxial sensor array without any defects. The frequency responses are firstly obtained for three different axial separations d , which is chosen as 2.54cm, 3.5cm and 4.5cm for 12-element sensor array. The data were acquired using Hewlett-Packard 4194A Impedance/Gain-Phase Analyzer as shown in Figure 4.3. The x-coordinate indicates the frequency normalized to 9.315MHz.

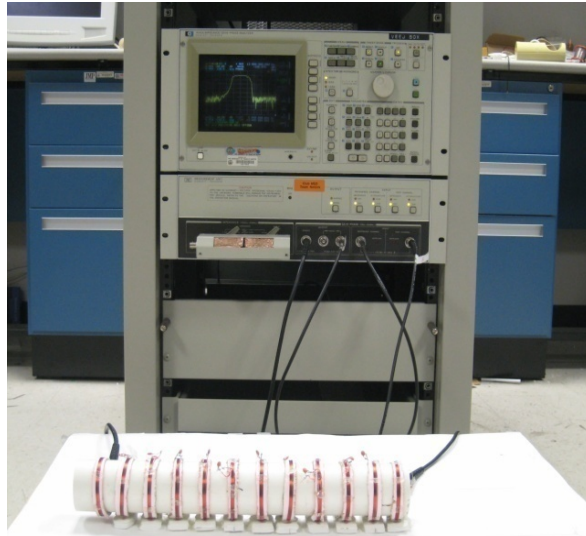


Figure 4.3 Experimental arrangement of 1-D coaxial sensor array

The insertion loss for 1-D coaxial sensor arrays ($d=2.54\text{cm}$) are presented in Figure 4.4. The simulated results taking one neighbors ($S=1$) and five neighbors ($S=5$) are compared with the measured results. The insertion loss curve with $S=5$ give better approximation about the frequency response. From the comparison, we can see that the real resistance in circuit is greater than our calculation ($R=0.3253\Omega$) which make the loss higher. Since the bandwidth is wider in experiment, the magnetic coupling between elements in this array is stronger than that we computed.

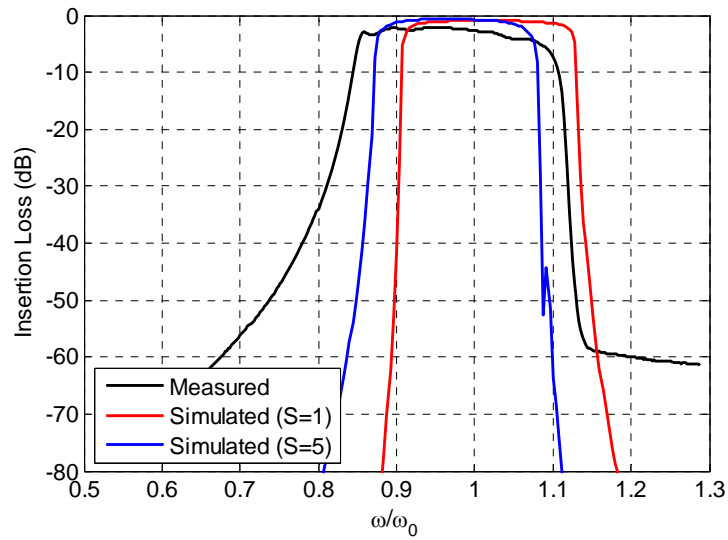


Figure 4.4 Insertion Loss vs. Normalized frequency of 1-D coaxial sensor array with $d=2.54\text{cm}$

The results for the sensor array constructed by same sensors with different spacing d are shown in Figure 4.5. All the three curves have bandpass shape. The passband are widened as the coupling between neighboring coils become stronger. The width of the passband is roughly proportional to the mutual inductance, as shown in Table 4.1. When the axial separation is greater, the linked flux will leak to the air instead of coupling to next coil which will also increase the loss.

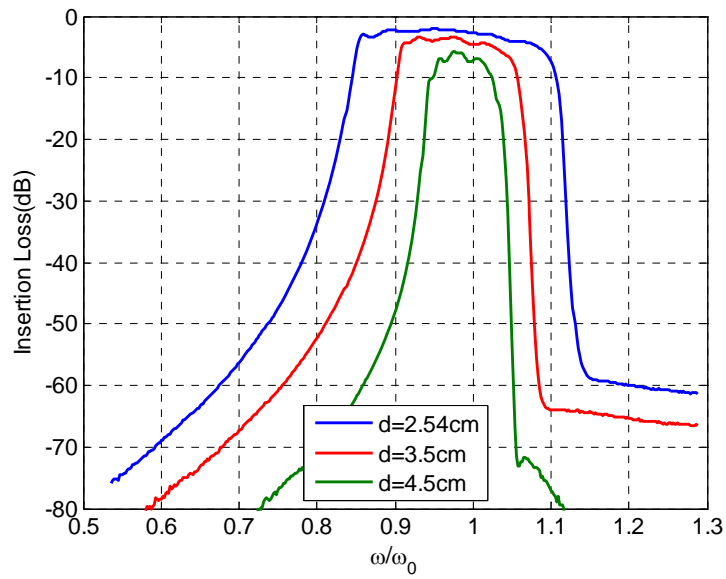


Figure 4.5 Insertion Loss vs. Normalized frequency for 1-D coaxial sensor array
($d=2.54\text{cm}$)

Table 4.1 Mutual inductance and measured bandwidth

Axial spacing $d(\text{cm})$	2.54	3.5	4.5
$M_1(\text{nH})$	313.74	187.76	116.4
Measure bandwidth $\Delta f(\text{KHz})$	2328.7	1397.2	838.3
$\Delta f M_1$	7.42	7.44	7.20

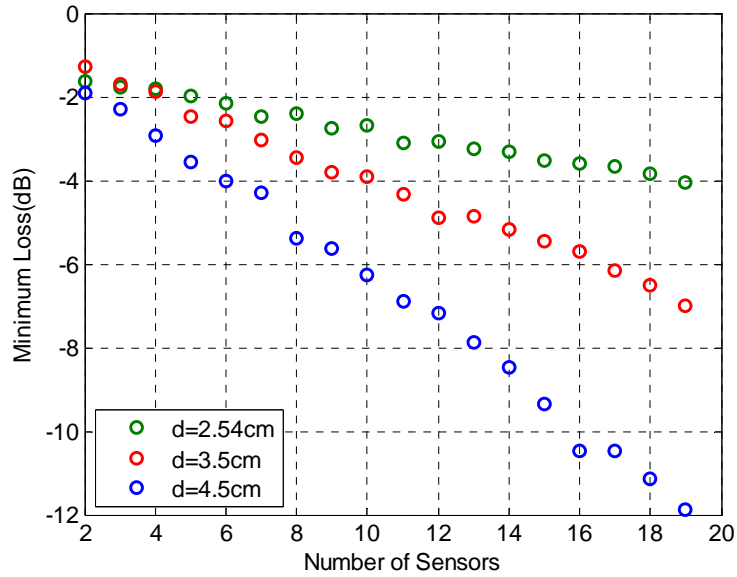


Figure 4.6 Minimum loss vs. Number of sensors of 1-D coaxial sensor array ($d=2.54\text{cm}$)

The measurement is also taken with different number of sensors. Axial spacing d is fixed and the number of sensors between driver and reader coils increase from 2 to 19. Figure 4.6 presents the variation of minimum loss as increased transmission line length. The test is repeated for different axial spacings. It shows that the minimum insertion loss for MI waveguides goes up almost linearly and stronger coupling between coils contribute to less insertion loss. With axial separation of 2.54cm, the average additional loss per tag is about 0.16dB, which for 3.5cm-sensor and 4.5cm-sensor array are 0.3dB and 0.58dB respectively.

4.3.2 Test of 1-D Corrosion Sensor Array with One Defect

In this part, the tested 12-element transmission line is built with 10 sensors between the driver and reader coils. One sensor circuit is open at one time. Figure 4.7

compare our calculation and measurement for 1-D axial sensor array ($d=2.54\text{cm}$) with only No.3 defect. It also shows that the resistance and mutual inductance is greater than our calculation.

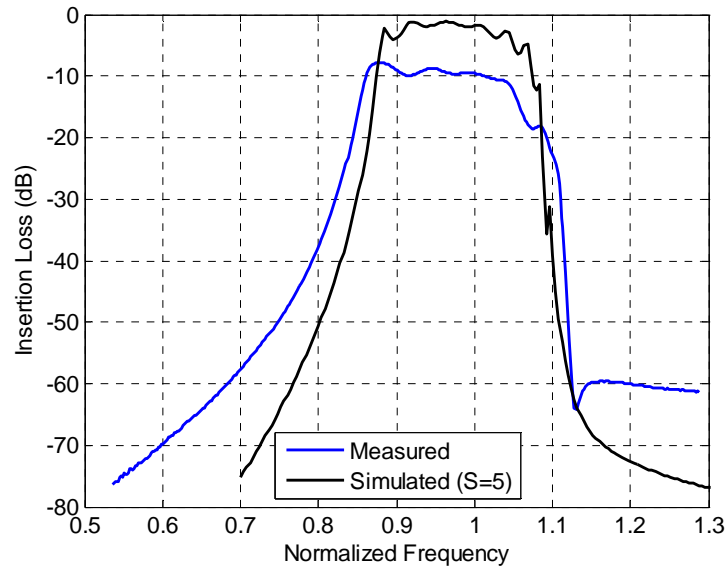


Figure 4.7 Insertion Loss vs. Normalized frequency for 1-D coaxial sensor array ($d=2.54\text{cm}$) with No.3 defect

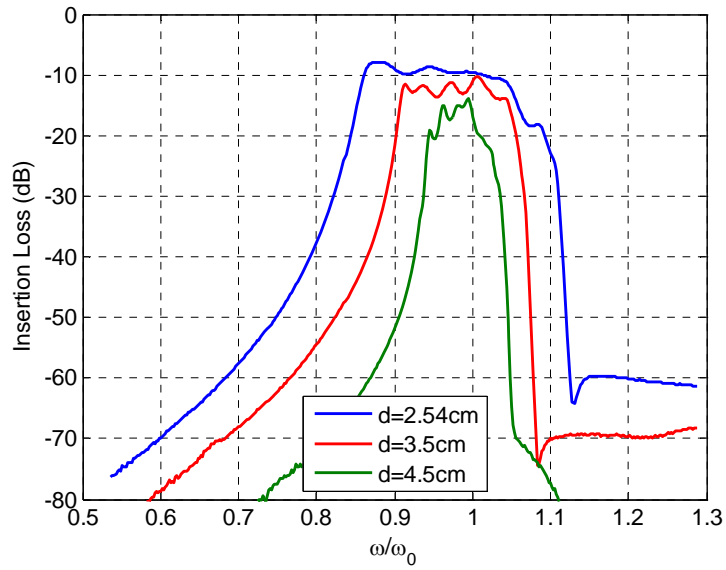


Figure 4.8 Insertion Loss vs. Normalized frequency for 1-D coaxial sensor array
($d=2.54\text{cm}$) with No.3 defect

Figure 4.8 compares the frequency response sensor array containing No.3 defect with different axial spacing. Narrower spacing contributes to wider bandwidth and smooth passband. The coaxial sensor array with $d=2.54\text{cm}$ is the best choice used to detect corrosion. Figure 4.9 presents the frequency variations with the 3rd, 5th, 7th and 9th element defect for coaxial sensor array ($d=2.54\text{cm}$). The passband is not as smooth as we simulated and unregular ripples are introduced. The loss during passband is increased about 5dB compared with the intact array. It is hard for us to identify which coil is open with the information of frequency response.

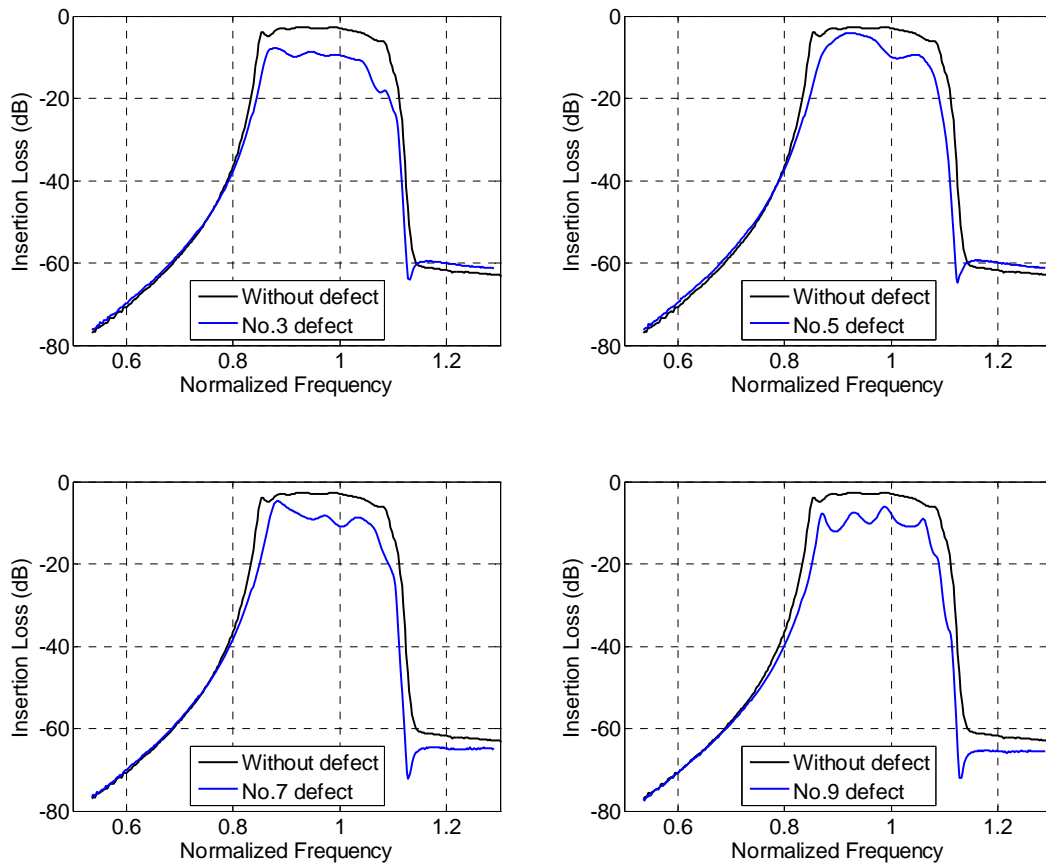


Figure 4.9 Insertion Loss vs. Normalized frequency for 1-D coaxial sensor array ($d=2.54\text{cm}$) with one defect

4.3.3 Test of 1-D Corrosion Sensor Array with Two Defects

The transmission line with two defects is tested. We cut off one more sensor circuit at the same time. The two defects will form a larger discontinuity or Fabry-Perot cavity. Figure 4.10 shows the frequency response of the sensor array ($d=2.54\text{cm}$) with the 3rd and 7th defect elements, and the 7th and 11th defect elements. Both set of peaks almost happen at the same frequency. If the 7th sensor is reference reflector, it is hard to

tell the difference between the two curves, and determining whether the 3rd or 11th element is broken.

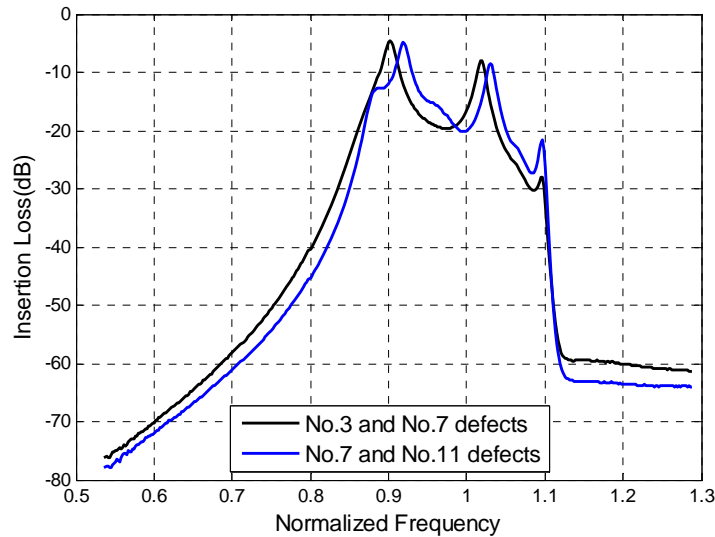


Figure 4.10 Frequency responses of 1-D coaxial sensor array ($d=2.54\text{cm}$) with two defects ($P=3$)

Based on the analysis above, the second element (the first sensor) is set intentionally as open. We cut off the circuit in another sensor and record frequency response of the MI waveguide.

Figure 4.11 presents the frequency variation results with different position of defect for 1-D axial sensor array ($d=2.54\text{cm}$). When the second defect is the nearest neighbor, it intensifies the mutual impedance discontinuity instead of forming a cavity. So no peaks appear and extra 15dB loss is introduced in the passband. Other plots in Figure 4.11 show the frequency characteristics for second defect at different positions for 1-D axial sensor array ($d=2.54\text{cm}$). Two, five and eight sensors are still intact respectively. We can see the two clear peaks in the passband in the second plot. For the

case of the eighth and eleventh sensor as the defect, the last peak is almost attenuated on high frequency edge of the passband. To avoid missing the peaks, the way is to check the frequency where peaks lie at by dispersion relationship.

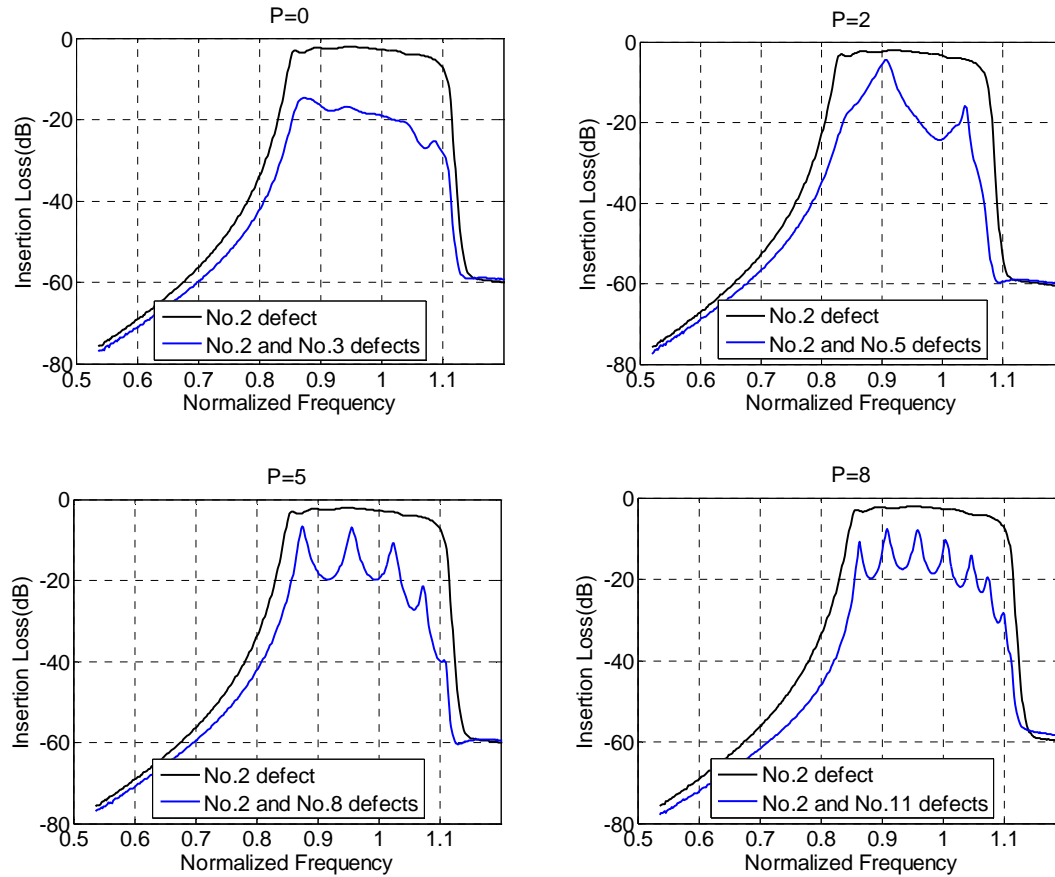


Figure 4.11 Insertion Loss vs. Normalized frequency for 1-D coaxial sensor array ($d=2.54\text{cm}$) with different sets of two defects

Since the last peak is not obvious while others can be detected, we record the frequency where clear peaks happen. If there are P sensors between two reflectors, then the peaks lie at frequency such that propagation coefficient satisfy $\beta d = n\pi/(P+1)$. For example, if P equals to 5, the value of βd should be $\pi/6, 2\pi/6, 3\pi/6, 4\pi/6, 5\pi/6$. Then given value of propagation coefficient βd , we can obtain corresponding frequency

and attenuation coefficient by dispersion relationship. To verify whether one more peak is attenuated at the high frequency edge, we compare the location of clear peaks with simulated value. For the sensor array with 2rd and 8th defects, there are four clear peaks during passband in Figure 4.11, which are compared with the simulated data for P at value of 4 and 5. Similarly, the locations of seven clear peaks are checked with the coaxial sensor array with a cavity containing 7 and 8 elements. To improve the accuracy, we take the interactions from nearest five neighbors into consideration. The results are shown in Figure 4.12. Both plots show that the $P-1$ clear peaks coincide with our simulation. The last peak can be predicted and will not be missed.

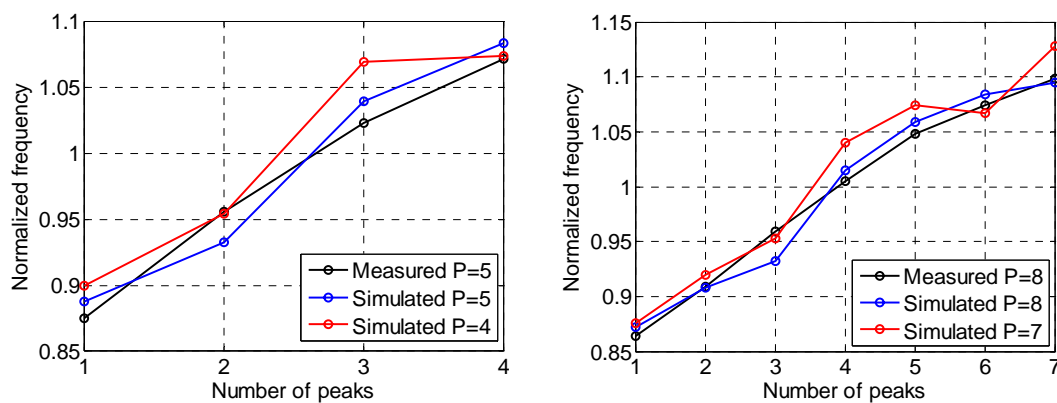


Figure 4.12 Verification of peaks locations for $P=5$ and $P=8$

4.4 Summary

In this chapter, we fabricate the passive wireless corrosion sensors and build the coaxial sensor array by the corrosion sensors with different spacing and number of elements. The minimum loss and frequency responses are compared. It shows that small spacing contributes to better performances. From the analysis and the experiment data

above, the onset of corrosion can be monitored by MIW with an intended defect sensor.

We can locate the corrosion exactly by computing the number of peaks.

CHAPTER 5 CONCLUSION

5.1 Motivation of Work

The objective of this thesis was to increase the ability and coverage of point corrosion sensors by building an inductively coupled sensor array. Research at UT in last few years has proven the effectiveness of point sensor in reflecting the local corrosion condition. The developed point corrosion sensors are used to construct the sensor array investigated in this thesis. Without interrogating point sensors individually, the sensor array can detect and locate the corrosion accurately and directly by one-off test, which is based on cavity resonance principle. The location of the corrosion can be decided by counting the peaks appearing in the passband. The results from the air test demonstrate the coaxial sensor array provides a convenient and effective means to monitor the corrosion in the structure.

There are still some limitations of the sensor net. The primary one is that the sensor net cannot contain many sensors as you want. As seen from Figure 4.11, more sensors would expect more possible peaks during the frequency band, which would increase error rate. Another one is the axial distance between the nearest coils could not be very far, since further spacing decrease the coupling factor and narrow the bandwidth and the frequency gap between peaks will be smaller. It makes us uneasy to find the exact number of peaks in a narrow passband. Some other environmental conditions and manufacturing tolerance may also introduce unexpected ripples or reflections in the

passband. The real peaks would be attenuated or hidden. All of these reasons would disturb or mislead our judgment of onset and location of corrosion.

5.2 Simulation and Results

5.2.1 Intact 1-D Corrosion Sensor Array

This simulation was conducted to learn about the frequency characteristics of the inductively coupled resonant sensor array, which can support magneto-inductive waves to propagate by the coupling between elements. A circuit model is provided to analyze both coaxial and coplanar sensor array. The dispersion relationship and insertion loss for both arrangement are calculated. The resonant sensor array acts as a bandpass filter. From this analysis, high coupling factor and quality factor would be required to obtain larger bandwidth and less insertion loss. Tests about the intact sensor array are done and the results coincide with our simulated data. Test for the sensor array with fixed spacing demonstrate that the insertion loss will be increased when more sensor are added to the array.

5.2.2 1-D Corrosion Sensor Array with One Defect

It has been shown that an array of resonant corrosion sensors act as a magneto-inductive waveguide. When one exposed wire is corroded broken, a mutual impedance discontinuity will be introduced by increased distance between the two elements. Greater strength of the discontinuity will introduced greater reflection, but the value of reflection coefficient varies slowly within the frequency band. The frequency characteristics are similar to that of intact sensor array but with extra loss and small

ripples. In simulation, if the defect is located far away the driver coil, more extra loss will be introduced. In experiment, the corrosion is simulated by cutting off the circuit directly. The ripples in the passband are greater we expect and it is almost impossible to differentiate which sensor circuit is open.

5.2.3 1-D Corrosion Sensor Array with Two Defects

The sensor array with two defects is further investigated. If two defects are adjacent, a much stronger discontinuity will be inside the MI waveguide. The extra loss is much greater than that of sensor array with one defect, since mutual inductance decrease sharply as the distance between two coils become greater. If the two defects are distributed that will form a Fabry-Perot cavity, the peaks will happen during the passband based on the cavity resonance principle. We choose the second element in the array as the reference reflector. When corrosion happened in another location, the corrosion can be located by extracting the number of peaks. The number of peaks equals to the number of intact sensors between the two discontinuities, as demonstrated in the experiments. But more sensors working between expect more peaks in the passband, and the peak would be attenuated at the high frequency edge. To avoid missing the peak and making wrong judgment, we compare the frequency where clear peaks lie at with our simulated value. This method is proven to be effective.

5.3 Recommendation for the Future

The open circuit is chosen as the reference reflector in the MI waveguide in the thesis. Future work can investigate other kinds of circuit as reference reflector to improve

the gap between peaks and troughs and last peak at the high frequency edge. This is also crucial in choosing the geometries of coils to have higher mutual factor and quality factor. Proper design will make the sensor array obtain a better frequency response and higher sensitivity in detecting corrosion. Furthermore extending the 1-D sensor array to be 2-D sensor net will have a greater coverage of infrastructure.

Bibliography

- [1] S. B. Chase and J. A. Laman, "Dynamics and Field Testing in the New Millennium: A Look Forward," Transportation in the New Millennium, Transportation Research Board, National Research Council 2000.
- [2] K. M. Grizzle, "Development of a Wireless Sensor Used to Monitor Corrosion in Reinforced Concrete Structures," M.S. Thesis, Dept of Civil Engineering, The University of Texas at Austin, 2003.
- [3] ASTM C876-91, "Standard Test Method for Half-cell Potentials of Uncoated Reinforcing Steel in Concrete," 1999.
- [4] S. Erdogdu, I. L. Kondratova, and T. W. Bremner, "Determination of Chloride Diffusion Coefficient of Concrete Using Open-circuit Potential Measurements," *Cement and Concrete Research*, vol. 34, pp. 603-609, 2004.
- [5] W. Morris, A. Vico, M. Vazquez, and S. R. de Sanchez, "Corrosion of Reinforcing Steel Evaluated by Means of Concrete Resistivity Measurements," *Corrosion Science*, vol. 44, pp. 81-99, 2002.
- [6] P. G. Cavalier and P. R. Vassie, "Investigation and Repair of Reinforcement Corrosion in a Bridge Deck," *Proc. Instn Civ. Engrs, Part 1*, vol. 72, pp. 401-419, 1982.
- [7] ASTM C597-83, "Standard Test Method for Pulse Velocity through Concrete," 1989.
- [8] B. Carkhuff and R. Cain, "Corrosion Sensors for Concrete Bridges," *Instrumentation & Measurement Magazine, IEEE*, vol. 6, pp. 19-24, 2003.
- [9] M. Saafi and P. Romine, "Embedded MEMS for Health Monitoring and Management of Civil Infrastructure," *Proceedings of SPIE, Smart Structures and Materials*, vol. 5391, pp. 331-343, 2004.
- [10] L. J. Novak, K. M. Grizzle, S. L. Wood, and D. P. Neikirk, "Development of State Sensors for Civil Engineering Structures," *Proceedings of SPIE, Smart Structures and Materials*, vol. 5057, pp. 358-363, 2003.
- [11] J. T. Simonen, M. M. Andringa, K. M. Grizzle, S. L. Wood, and D. P. Neikirk, "Wireless Sensors for Monitoring Corrosion in Reinforced Concrete Members," *Proceedings of SPIE, Smart Structures and Materials*, vol. 5391, pp. 587-596, 2004.

- [12] P. Pasupathy, M. Zhuzhou, D. P. Neikirk, and S. L. Wood, "Unpowered Resonant Wireless Sensor Nets for Structural Health Monitoring," in *Sensors, 2008 IEEE*, 2008, pp. 697-700.
- [13] P. R. Nainani, "Optimization of Passive Wireless Concrete Corrosion Sensors Using the Genetic Algorithm," M.S. Thesis, Dept of Electrical and Computer Engineering, The University of Texas at Austin, 2004.
- [14] P. Pasupathy, S. Munukutla, D. P. Neikirk, and S. L. Wood, "Versatile wireless sacrificial transducers for electronic structural surveillance sensors," in *Sensors, 2009 IEEE*, 2009, pp. 979-983.
- [15] <http://www.vatechnologies.com/eciIndex.htm>.
- [16] <http://www.tinyos.net>.
- [17] R. Szewczyk, A. Mainwaring, J. Polastre, J. Anderson, and D. Culler, "An analysis of a Large Scale Habitat Monitoring Application," in *Proceedings of the 2nd international conference on Embedded networked sensor systems* Baltimore, MD, USA: ACM, 2004.
- [18] S. Kim, S. Pakzad, D. E. Culler, J. Demmel, G. Fenves, S. Glasser, and M. Turon, "Health Monitoring of Civil Infrastructures Using Wireless Sensor Networks," EECS Department, University of California, Berkeley 2006.
- [19] <http://www.tinyos.net/scoop/special/hardware>.
- [20] M. M. Andringa, D. P. Neikirk, N. P. Dickerson, and S. L. Wood, "Unpowered Wireless Corrosion Sensor for Steel Reinforced Concrete," in *Sensors, 2005 IEEE*, 2005, pp. 155-158.
- [21] M. M. Andringa, "Unpowered Wireless Sensors for Structural Health Monitoring," 2006.
- [22] Andringa, M. Matthew, Puryear, M. John, Neikirk, P. Dean, Wood, and L. Sharon, "Low- cost Wireless Corrosion and Conductivity Sensors," *Proceedings of SPIE, Smart Structures and Materials* vol. 6174I, 2006.
- [23] F. Grover, *Inductance Calculations: Working Formulas and Tables*: New York: Dover, 1973.
- [24] <http://www.rippylon.com/BiotSavart/bsov.pdf>.
- [25] E. Shamonina, V. A. Kalinin, K. H. Ringhofer, and L. Solymar, "Magneto-inductive waveguide," *Electronics Letters*, vol. 38, pp. 371-373, 2002.

- [26] E. Shamonina, V. A. Kalinin, K. H. Ringhofer, and L. Solymar, "Magnetoinductive waves in one, two, and three dimensions," *Journal of Applied Physics*, vol. 92, pp. 6252-6261, 2002.
- [27] R. R. A. Syms, E. Shamonina, and L. Solymar, "Magneto-inductive waveguide devices," *Microwaves, Antennas and Propagation, IEE Proceedings -*, vol. 153, pp. 111-121, 2006.
- [28] Pasupathy, P, Neikirk, P. Dean, Wood, and L. Sharon, "Improved reading techniques for electronic structural surveillance tags," *Proceedings of SPIE, Smart Structures and Materials*, vol. 6932, 2008.

Vita

Ye Chen was born on 27 Jan 1986 in Shangrao, China, the daughter of Chun Sheng Chen and Xiao Tao Li. Ye attended Poyang No.1 Middle School and graduated in May of 2001. In September of 2001, Ye began her undergraduate study and received her B.E. degrees in Electrical Engineering from Tongji University four years later. She then was enrolled in Chinese Academy of Sciences and become a graduate student in Institute of Acoustics. She was granted Master's degree at May, 2008. In September of 2008, she entered the Department of Electrical and Computer Engineering at the University of Texas at Austin to continue her graduate study and began working with Dr. Dean Neikirk in June, 2009.

Permanent address: 3517 North Hills Dr. Apt. V104

Austin, TX 78731

This thesis was typed by the author.